



Full Text View

[Volume 32, Issue 8 \(August 2002\)](#)

Journal of Physical Oceanography

Article: pp. 2379–2404 | [Abstract](#) | [PDF \(2.75M\)](#)

Dynamics of the Pacific Subsurface Countercurrents^{*}

Julian P. McCreary Jr.

International Pacific Research Center, University of Hawaii, Honolulu, Hawaii

Peng Lu

Oceanographic Center, Nova Southeastern University, Dania, Florida

Zuojun Yu

International Pacific Research Center, University of Hawaii, Honolulu, Hawaii

(Manuscript received May 29, 2001, in final form February 4, 2002)

DOI: 10.1175/1520-0485(2002)032<2379:DOTPSC>2.0.CO;2

ABSTRACT

A hierarchy of models, varying from 2½-layer to 4½-layer systems, is used to explore the dynamics of the Pacific Subsurface Countercurrents, commonly referred to as “Tsuchiya Jets” (TJs). The TJs are eastward currents located on either side of the equator at depths from 200 to 500 m and at latitudes varying from about 2° to 7° north and south of the equator, and they carry about 14 Sv of lower-thermocline (upper-intermediate) water throughout the tropical Pacific. Solutions are found in idealized and realistic basins and are obtained both analytically and numerically. They are forced by winds and by a prescribed Pacific interocean circulation (IOC) with transport M (usually 10 Sv), representing the outflow of water in the Indonesian passages and a compensating inflow from the Antarctic Circumpolar Current.

Analytic solutions to the 2½-layer model suggest that the TJs are geostrophic currents along arrested fronts. Such fronts are generated when Rossby wave characteristics, carrying information about oceanic density structure away from boundaries, converge or intersect in the interior ocean. They indicate that the southern and northern TJs are driven by upwelling along the South American coast and in the ITCZ band, respectively, that the northern TJ is strengthened by a recirculation gyre that extends across the basin, and that TJ pathways are sensitive to stratification parameters. Numerical solutions to the 2½-layer and 4½-layer models confirm the analytic results, demonstrate that the northern TJ is strengthened considerably by unstable waves along the eastward branch of the recirculation gyre, show that the TJs are an important

Table of Contents:

- [Introduction](#)
- [The model oceans](#)
- [Solutions to the 2½-layer](#)
- [Solutions to the 4½-layer](#)
- [Summary and discussion](#)
- [REFERENCES](#)
- [FIGURES](#)

Options:

- [Create Reference](#)
- [Email this Article](#)
- [Add to MyArchive](#)
- [Search AMS Glossary](#)

Search CrossRef for:

- [Articles Citing This Article](#)

Search Google Scholar for:

- [Julian P. McCreary](#)
- [Peng Lu](#)
- [Zuojun Yu](#)

branch of the Pacific IOC, and illustrate the sensitivity of TJ pathways to vertical-mixing parameterizations and the structure of the driving wind.

In a solution to the 2½-layer model with $M = 0$, the southern TJ vanishes but the northern one remains, being maintained by the unstable waves. In contrast, both TJs vanish in the $M = 0$ solution to the 4½-layer model, apparently because wave energy can radiate into a deeper layer (i.e., layer 4). In the 4½-model, then, the TJs exist because of the Indonesian Throughflow, a remarkable example of remote forcing on a basinwide scale.

1. Introduction

a. Observations

The Pacific Subsurface Countercurrents are narrow currents that flow eastward along the thermal fronts at the poleward edges of thermostad water (Fig. 1). They were first reported by Tsuchiya (1972, 1975, 1981) and are now commonly referred to as Tsuchiya jets (TJs). Their basic properties have been recently summarized by Johnson and Moore (1997) and Rowe et al. (2000), based on hydrographic and acoustic Doppler current profile (ADCP) data, respectively. The two jets carry about 14 Sv of water across the basin, with the northern jet being somewhat stronger than the southern one. Over much of the basin the southern TJ, in fact, appears to consist of two distinct branches, a “primary” one closer to the equator that is shallower and stronger than a “secondary” one farther away (Fig. 1). The jets rise in the water column as they cross the basin, their current cores shoaling from about 300 m in the western ocean to 150 m in the east. As they shoal, their core densities decrease, suggesting that diapycnal processes are involved in their dynamics. In individual ADCP sections, the jets are very narrow (only about 1.5° wide), attain peak speeds of 30–40 cm s⁻¹, are associated with a jump in potential vorticity across their current core, and are flanked by westward flows.

Figure 2 illustrates the horizontal structure of the TJs, showing acceleration potential relative to 900 dbar on the 26.5 kg m⁻³ neutral density surface, which lies near the jet cores (Johnson and McPhaden 1999; see Reid 1965, for a similar map on the 125 cl ton⁻¹ density surface). The shaded areas indicate regions of cyclonic flow in each hemisphere, and the TJs are the eastward flows on their equatorward sides. Note that the TJs shift away from the equator toward the east, a well-known property first noted by Tsuchiya (1972, 1975). The northern TJ does not appear to extend to the eastern boundary but rather to recirculate in the interior ocean. In contrast, the southern TJ does extend to the eastern boundary, the 11.5 J kg⁻¹ line intersecting the coast near 12°S. The gradient of acceleration potential across the northern TJ is considerably sharper than in the Southern Hemisphere, perhaps an indication of the southern jet having two branches.

Although the TJs themselves are equatorially confined, their cool temperature indicates that their source water lies well outside the Tropics. Tsuchiya (1981) argued that it is actually formed northeast of New Zealand, and Toggweiler et al. (1991) suggested that upper Antarctic Intermediate Water is another possible source. Throughout this paper, we refer to either of these water mass types as South Pacific lower-thermocline water (SPLTW). The SPLTW circulates westward and northward about the South Pacific subtropical gyre, moves to the equator within the lower portion of the New Guinea Coastal Undercurrent (Tsuchiya et al. 1989; Tsuchiya 1991), and some of it then turns eastward near the equator to supply much of the water for the TJs. Bingham and Lukas (1995) and Johnson and Moore (1997) also note the contribution of fresher Northern Hemisphere water, but only on the northern flank of the northern TJ.

The sink regions of the jets are less clear. Figure 2 suggests that at least a portion of the southern-jet water feeds the Peru–Chile coastal undercurrent and likely upwells along the coast there, where sea surface temperature can be as low as 15°C (Lukas 1986; Toggweiler et al. 1991). The property that the northern TJ recirculates in the northern Tropics suggests that it upwells in the interior ocean in regions of Ekman suction associated with the intertropical convergence zone (ITCZ). In support of this idea, Kessler (2001, personal communication) used hydrographic and expendable bathythermograph data to investigate the circulation in the vicinity of the Costa Rica Dome (8°N, 90°W), a region where the northern TJ abruptly turns northward. His analyses indicated that about half of the 6 Sv transport (Sv ≡ 10⁶ m³ s⁻¹) of the TJ upwells through the thermocline, driven by the upwelling favorable wind curl there, and the rest turns westward to join the lower part of the North Equatorial Current (NEC). Rowe et al. (2000) argued that part of the TJs in both hemispheres turns equatorward in the eastern ocean to join the Equatorial Intermediate Current (EIC), a westward equatorial current usually located beneath the Equatorial Undercurrent (EUC) (but not present in Fig. 1).

b. Models

Dynamically, the TJs remain one of the least understood of large-scale oceanic currents: Neither the processes that maintain them, nor their role in the Pacific general circulation are yet clear.

In [McPhaden's \(1984\)](#) and [McCreary's \(1981\)](#) solutions to continuously stratified, vertically diffusive, linear models, eastward currents resembling the TJs appear as downward-bending lobes attached to the EUC. [McPhaden \(1984\)](#) explained the lobes as resulting from a balance between vertical diffusion of cyclonic relative vorticity and advection of planetary vorticity, that is, primarily a local balance in which energy for the lobes is supplied by the zonal wind. In the [McCreary \(1981\)](#) model, the lobes almost vanish when the basin has no eastern boundary, suggesting that remote forcing by reflected Rossby waves is also essential for their existence. [[McCreary \(1981\)](#) only commented that the EIC vanished in a solution without an eastern boundary. We repeated this solution to confirm that the lobes also disappear.] One limitation of both solutions is that, in contrast to the observed TJs, the lobes are not distinctly separate from the EUC. Another is that the water that flows in them originates by downwelling within the Tropics, rather than in the South Pacific.

Recently, [Marin et al. \(2000\)](#) developed a local two-dimensional (y - z) model for the TJs. A background density structure $\rho_b(y, z)$ is imposed with a pycnocline that rises and sharpens near the equator, similar to the observed one, and density is relaxed back to ρ_b in and above the pycnocline with a timescale of 12 days. The system attempts to generate a zonal velocity field in geostrophic balance with ρ_b and, in so doing, drives an ageostrophic meridional circulation. Poleward flows are established just below the pycnocline that carry near-equatorial water parcels poleward. The parcels conserve their angular momentum and consequently produce strong eastward jets near $\pm 3^\circ$, the model TJs. A limitation of the study is that rather severe restrictions are required to reduce the 3D equations to a 2D form. Nevertheless, it does focus attention on the potential importance of local processes in TJ dynamics.

[Johnson and Moore \(1997\)](#) used a 1½-layer model, in which the active layer represented the thermostad region, to simulate the property that the TJs diverge from the equator as they flow eastward. They assumed that the layer thickened to the east as the thermostad region does in the real ocean, forced the model by prescribing a jetlike inflow near the equator at the western boundary (or, equivalently, a sink at the eastern boundary), and solved for the resulting inviscid flow field throughout the interior ocean. The solution had an interior jet that diverged from the equator, a consequence of conservation of potential vorticity, $(f - u_y)/h$, which caused the jets to shift poleward as they flowed into a region of thicker h . In contrast to [Marin et al. \(2000\)](#), the [Johnson and Moore \(1997\)](#) study supports the idea that the TJs are a remotely forced inviscid flow, not directly forced by the local wind. It does not, however, provide an answer as to their actual forcing mechanism since their solution is forced by an externally prescribed boundary condition.

[Lu et al. \(1998\)](#) and [McCreary and Lu \(2000\)](#) used 3½-layer and 4½-layer models, respectively, to study the Pacific general circulation. In both studies, solutions were forced by [Hellerman and Rosenstein \(1983\)](#) annual-mean winds. They were also forced by a specified inflow into the basin across the southern boundary from the Antarctic Circumpolar Current and a compensating outflow from layers 1 and 2 along the western boundary just north of the equator. This mass exchange simulated the Pacific interocean circulation (IOC) in which water enters the basin in the South Pacific, crosses the equator, is entrained into surface layers, and finally leaves the Pacific through the Indonesian passages as surface or thermocline water. Associated with the IOC, solutions had an eastward-flowing branch along the equator in layer 3, the models' thermostad layer. This current began to diverge weakly into two cores in the central ocean, a result of potential vorticity conservation [as in the [Johnson and Moore \(1997\)](#) model]. However, the cores never diverged sufficiently far to form distinct TJs, and most of the layer-3 water upwelled into layer 2 well before it reached the eastern ocean.

Realistic TJs have been simulated in solutions to general circulation models (GCMs) only recently, likely due to improved resolution ([Maltrud et al. 1998](#); [Ishida et al. 1998](#)). [See [Kitamura and Sugimoto \(1987\)](#) for a discussion of an earlier GCM solution with weak TJs.] They are particularly well represented in the [Ishida et al. \(1998\)](#) study, which utilizes the highly vertically resolved (55 levels) Japan Marine Science and Technology Center (JAMSTEC) GCM. [Donahue et al. \(2002\)](#) discuss the TJs in the JAMSTEC solution in detail, demonstrating that they have many of the observed attributes reported in [Rowe et al. \(2000\)](#), including a weak secondary southern jet. Its primary TJs appear to be associated with near-equatorial, horizontal recirculations [similar to, but stronger than, those present in the [Lu et al. \(1998\)](#) solution]. Large-amplitude unstable waves and eddies are prominent along these recirculations, and it is not clear whether they are generated by, or the cause of, the mean flows. It is noteworthy that the solution's primary TJs do not diverge from the equator (although the secondary one does), supporting the idea that they are largely an equatorially trapped phenomenon.

c. Present research

In this study, we utilize an hierarchy of ocean models to simulate the TJs, to investigate the processes that maintain them, and to understand their role in the Pacific general circulation. The models are constant-density, 2½-layer or 4½-layer systems. (We also utilized a 3½-layer model during this research, but eventually abandoned it in favor of the 4½-layer one; see [section 4](#).) Solutions are found in idealized, rectangular half-basins and in a realistic domain extending from 30°S to 30°N. They are forced by idealized and realistic winds and by a prescribed mass exchange that represents the IOC.

Our major conclusion is that the TJs are arrested fronts, like those discussed by [Dewar \(1991, 1992\)](#). These fronts are generated in regions where Rossby wave characteristics converge or intersect in the interior ocean, a dynamical situation similar to that inherent in the [Johnson and Moore \(1997\)](#) solution. Other results are that the primary source of water for the

TJs is SPLTW, that their sinks are coastal upwelling along South America and open-ocean upwelling by Ekman suction in the ITCZ band, and that the TJs are an important branch of the IOC.

2. The model oceans

The numerical models in our hierarchy are straightforward modifications of the 3½-layer and 4½-systems of [Lu et al. \(1998\)](#) and [McCreary and Lu \(2001\)](#). For this reason, only model aspects most relevant for our present purposes are discussed here.

a. The 4½-layer model

1) LAYER STRUCTURE

[Figure 3](#) schematically illustrates the structure of the 4½-layer model, showing a meridional section at 140°W from our main run reported in [section 4](#). It consists of four active layers with thicknesses h_i , velocities $\mathbf{v}_i = (u_i, \mathbf{v}_i)$, and temperatures T_i ($i = 1, 2, 3, 4$ is a layer index), overlying a deep, inert layer of density T_d where the pressure-gradient field vanishes. The temperatures are kept fixed, and unless specified otherwise are $T_i = (28, 20, 11, 8)^\circ\text{C}$ and $T_d = 5^\circ\text{C}$. Layer densities are determined from temperatures by the relation $\rho_i = \rho_o(1 - \alpha T_i)$, where $\rho_o = 1 \text{ g cm}^{-3}$ and $\alpha = 2.5 \times 10^{-4} \text{ }^\circ\text{C}^{-1}$. The water that flows in layers 2 and 3 originates primarily from subtropical subduction and the IOC, respectively, so we interpret them as corresponding to thermocline water and SPLTW. Layer-4 water represents upper-intermediate water.

2) ACROSS-INTERFACE VELOCITIES

Water can move across the interfaces beneath the upper three layers at the velocities $w_1, w_2,$ and w_3 . These velocities are a crucial part of the model's physics, because they represent all the vertical mixing processes that allow water to rise or descend in the water column. They are given by

$$\begin{aligned}
 w_1 &= w_{e1} + w_d - \delta w_{c2} \theta(h_1 - h_{e1}) \\
 w_2 &= w_{e2} + (1 - \delta) w_{c2} \theta(h_1 - h_{e1}) \\
 &\quad - \epsilon w_{c3} \theta(h_2 - h_{e2}) \\
 w_3 &= w_{c3} [\theta(h_{e2} - h_2) + (1 - \epsilon) \theta(h_2 - h_{e2})] \\
 &\quad + w_{m3} - w_{c4},
 \end{aligned} \tag{1}$$

where w_{ei} and w_d parameterize the processes of upwelling and subduction, the w_{ci} terms are correction velocities that prevent layers from becoming thinner than specified minimum values, and the θ functions are step functions that specify when the correction terms act. Unless stated otherwise, $\delta = \epsilon = 1$. No water is allowed to transfer across the bottom of layer 4; that is, $w_4 = 0$. This restriction ensures that mass is conserved in the system and that the total transport can adjust toward Sverdrup balance.

According to the [Kraus and Turner \(1967\)](#) model, wind stirring will entrain water into the mixed layer whenever it becomes sufficiently thin. We parameterize this process by

$$\begin{aligned}
 w_{e1} &= \frac{(h_1 - h_{e1})^2}{h_{e1} t_e} \theta(h_{e1} - h_1), \\
 w_{e2} &= \frac{(h_2 - h_{e2})^2}{h_{e2} t_e} \theta(h_{e2} - h_2) \theta(h_{e1} - h_1),
 \end{aligned} \tag{2}$$

where $h_{e1} = h_{e2} = 40 \text{ m}$ and $t_e = 0.2 \text{ days}$. With this specification for w_{e2} , layer 2 essentially becomes part of the surface mixed layer when $h_1 + h_2 \leq h_{e1} + h_{e2}$.

We parameterize subduction by

$$w_d = -\frac{(h_1 - h_d)^2}{h_d t_d} \theta(h_1 - h_d) \theta(|y| - y_d) \quad (3)$$

and set $t_d = 180$ days, $h_d = 80$ m, and $y_d = 15^\circ$. According to (3), subduction is represented by a transfer of water from layer 1 to layer 2 whenever h_1 becomes thicker than a specified thickness h_d . It occurs only at latitudes poleward of $\pm y_d$, because little subduction is expected to occur in the tropical ocean where warm water extends to about 15° north and south of the equator (the warm pool) and SST is basically uniform.

The correction terms w_{ci} are included to prevent layers from thinning to zero thickness. They have the form

$$w_{ci} = \frac{(h_{ci} - h_i)^2}{h_{ci} t_i} \theta(h_{ci} - h_i), \quad (4)$$

with $t_i = t_e$, $h_{c2} = h_{c4} = 40$ m, and $h_{c3} = 25$ m. According to (4), the corrections become active only when dynamical processes attempt to make h_i thinner than minimum thicknesses h_{ci} . Because currents are large in thin layers, (4) can be viewed as being a simple parameterization of the strong mixing that occurs whenever the Richardson number becomes small. (Note that w_{e1} and w_{e2} are essentially correction terms, labeled differently because they parameterize a different physical process.) With the choices $\delta = \epsilon = 1$, the switching by the step functions in (1) ensures that w_{ci} detrains from layer $(i - 1)$, if that layer is not too thin, and entrains from layer $(i + 1)$ if it is.

Using only the preceding across-interface velocities, solutions can develop realistic equatorial circulations with TJs. The thickness of the upper three layers, however, is somewhat too thin in the Tropics because the velocities do not act until individual layers become thinner than their minimum values [see section 4a(4)]. To overcome this limitation, we include the additional across-interface velocity

$$w_{m3} = \kappa \left(\frac{1}{h_3} - \frac{\mathcal{H}_4}{\mathcal{H}_3} \frac{1}{h_4} \right), \quad (5)$$

where \mathcal{H}_3 and \mathcal{H}_4 are the initial layers thicknesses defined below and, unless stated otherwise, $\kappa = 0.02 \text{ cm}^2 \text{ s}^{-1}$. This term parameterizes diapycnal mixing in the deep ocean and is based upon a steady-state balance between heat diffusion and vertical advection (Lu et al. 1998). According to (5), there is diapycnal mixing whenever ocean dynamics forces the ratio h_3/h_4 away from $\mathcal{H}_3/\mathcal{H}_4$. Note that w_{m3} is positive where h_3 is relatively thin, and it is in these regions that layer-4 water mixes upward into layer 3.

3) BASIN AND BOUNDARY CONDITIONS

The model basin, shown in Figs. 4, 10a, and 10b, is a representation of the Pacific basin extending from 30°S to 30°N , 125°E to 70°W . Closed, no-slip conditions, $u_i = v_i = 0$, are imposed on all basin boundaries. To include the IOC, inflow is allowed through a segment of the southern boundary from 154°E to 164°E (adjacent to the southwestern corner of the basin) and outflow is allowed through the western boundary from 2°N to 6°N . Specifically, the closed conditions are modified along the southern segment by setting

$$v_3 = \phi \frac{M}{h_3 L_S}, \quad v_4 = (1 - \phi) \frac{M}{h_4 L_S}, \quad (6a)$$


and changed along the western boundary segment to

$$u_1 = u_2 = -\frac{M}{(h_1 + h_2) L_W}, \quad (6b)$$

where M is the specified interocean transport, $L_S = 1110$ km and $L_W = 440$ km. Conditions (6a) and (6b) require that the model Indonesian Throughflow leaves the Pacific in layers 1 and 2, whereas the compensating inflow is in layers 3 and 4.

Unless specified otherwise, $\Phi = 0.8$, so that most of the inflow is in layer 3.

4) FORCING AND NUMERICS

Unless specified otherwise, solutions are forced by a modified version of [Hellerman and Rosenstein's \(1983\)](#) climatological monthly-mean wind stresses ([Fig. 4](#) ) and by the boundary inflow and outflow M . The zonal component of the [Hellerman and Rosenstein \(1983\)](#) winds τ^x is believed to be too strong near the equator by about 30% ([Harrison 1989](#)). To correct for this deficiency, we replaced τ^x with $\tau^x(x, y) - \Delta\tau(x)$ throughout the domain, where $\Delta\tau = (0.3/L) \int_{-L/2}^{L/2} \tau^x dx$ and $L = 10^\circ$ a change that weakens equatorial τ^x but does not affect wind curl ([Yu et al. 2000](#)). Transport M is usually set to 10 Sv, a value consistent with estimates of the Indonesian Throughflow transport from observations and from the ‘‘Island Rule’’ ([Godfrey 1989](#)).

Solutions are evaluated on a standard Arakawa C-grid in rectangular coordinates with the resolution $\Delta x = \Delta y = 0.25^\circ$. Both Laplacian and biharmonic mixing are included with coefficients $\nu = 2 \times 10^7 \text{ cm}^2 \text{ s}^{-1}$ and $\nu_4 = 10^{20} \text{ cm}^4 \text{ s}^{-1}$. To broaden the northern and southern boundary currents, ν is four times its interior value within 5° of each boundary and linearly ramped to the interior value in the next 5° . To ensure model stability during the initial spinup, ν is increased to $3 \times 10^7 \text{ cm}^2 \text{ s}^{-1}$ for the first 20 years of the integration.

Initial layer thickness are $\mathcal{H}_1 = 40 \text{ m}$, $\mathcal{H}_2 = 40 \text{ m}$, $\mathcal{H}_3 = 250 \text{ m}$, and $\mathcal{H}_4 = 350 \text{ m}$. However, because the w_i allow mass exchange between layers, there is really only one independent parameter among the four; the total initial thickness $\mathcal{H} = \sum_{i=1}^4 \mathcal{H}_i$, say. Solutions are obtained by integrating the model at least 100 years from a state of rest, by which time they have approached equilibrium.

b. The 2½-layer model

The 2½-layer numerical model differs from the 4½-layer one in that it has only two active layers, $w_1 = w_{e1} - w_{c2}$, $w_2 = 0$, $h_{e1} = \mathcal{H}_1 = 80 \text{ m}$, and $\mathcal{H} = \mathcal{H}_1 + \mathcal{H}_2$ is either 1000 m or 300 m. In addition, to be consistent with the analytical model described below, the advection terms in the momentum equations are dropped (except for one reported test solution), but solutions are not fundamentally changed if they are retained. Unless specified otherwise, $T_1 = 25^\circ\text{C}$, $T_2 = 11^\circ\text{C}$, and $T_d = 5^\circ\text{C}$. Solutions are forced by idealized representations of the southeast and northeast trades, as described in [sections 3b](#) and [3c](#), and by an IOC transport M that is usually set to 5 Sv, that is, half the full-basin value.

Solutions are obtained in either of two rectangular half-basins, which extend zonally from 0° to 100° and meridionally from the equator either to 30°S (the ‘‘southern’’ half-basin) or 30°N (the ‘‘northern’’ half-basin). Symmetric boundary conditions, $u_{iy} = 0$, $\mathbf{v}_i = 0$, are imposed along the equator and closed, no-slip conditions are imposed elsewhere. For the southern half-basin, these conditions are modified along the southern boundary from 0° to 10° by setting

$$v_2 = \frac{M}{h_2 L_S}, \quad (7a)$$

and along the equator from 0° to 5° to

$$v_1 = \frac{M}{h_1 L_S}. \quad (7b)$$

For the northern half-basin, [\(7a\)](#) is applied along the equator from 0° to 5° lon and

$$u_1 = -\frac{M}{h_1 L_W} \quad (7c)$$

is imposed along the western boundary from 2° to 6°N . The horizontal resolution and mixing are the same as for the 4½-layer model, except that ν is not increased near the equatorial boundary. Typically, solutions are spun up for a period of 61 years, and plots are either instantaneous or 360-day averaged plots from that year.

Analytic solutions are found to a simplified version of the 2½-layer model that is steady state, inviscid, and neglects

momentum advection. Equations of motion in each layer are

$$\begin{aligned} -fv_1 + p_{1x} &= \tau^x/h_1, & fu_1 + p_{1y} &= \tau^y h_1, \\ (h_1 u_1)_x + (h_1 v_1)_y &= w', \end{aligned} \quad (8a)$$

$$\begin{aligned} -fv_2 + p_{2x} &= 0, & fu_2 + p_{2y} &= 0, \\ (h_2 u_2)_x + (h_2 v_2)_y &= -w', \end{aligned} \quad (8b)$$

where layer pressures are

$$p_1 = g'_{12} h_1 + g'_{23} h, \quad p_2 = g'_{23} h, \quad (8c)$$

$h = h_2 + h_2$, $g'_{ij} = g(\rho_j - \rho_i)/\rho_0$, and $\rho_3 = \rho_d$. Velocity w'_1 is an entrainment rate (i.e., $w'_1 \geq 0$) caused by wind-driven upwelling, either coastal upwelling along the eastern boundary or open-ocean upwelling via Ekman suction. It acts instantaneously to prevent h_1 from ever becoming thinner than h_{e1} , essentially given by w_{e1} in the limit $t_e \rightarrow 0$. Boundary conditions differ from those for the numerical model, and they are specified in [sections 3b](#) and [3c](#).

3. Solutions to the 2^{1/2}-layer model

In this section, we report idealized solutions that identify basic TJ dynamics. We begin with an overview of theoretical ideas that help to understand properties of our solutions, and then discuss the southern and northern TJs separately since their dynamics differ significantly.

a. Theory

1) CHARACTERISTIC CURVES

In regions where $w'_1 = 0$, [Eq. \(8\)](#) yields a single equation for h ,

$$\mathbf{v}_g h_y + (\bar{u}_g - c_r) h_x = 0, \quad (9)$$

where

$$\begin{aligned} \bar{u}_g &= -\frac{1}{h} \left(\Psi_y + \frac{\tau^y}{f} \right), \\ \bar{v}_g &= \frac{1}{h} \left(\Psi_x + \frac{\tau^x}{f} \right) = \frac{f}{h\beta} w_{\text{Ek}} \end{aligned} \quad (10)$$

are the depth-averaged, zonal and meridional geostrophic currents in the two active layers, $\Psi = (1/\beta) \int_{x_e}^x \text{curl} \tau dx$ is the Sverdrup transport streamfunction, $w_{\text{Ek}} = \text{curl}(\tau/f)$ is the Ekman pumping velocity, $c_r = (\beta/f^2) g'_{12} (h_1 h_2/h)$, $\beta = f_y$, and $x_e(y)$ is the location of the eastern boundary ([Luyten et al. 1983](#); [Luyten and Stommel 1986](#)).

According to [\(9\)](#), h is constant along characteristic curves, $x_c(s)$ and $y_c(s)$, obtained by integrating the equations

$$\frac{dx_c}{ds} = \bar{u}_g - c_r, \quad \frac{dy_c}{ds} = \bar{v}_g, \quad (11)$$

where s is a timelike variable. The integration requires that h and h_1 are specified on some boundary of the domain and that h_1 (and hence $h_2 = h - h_1$) is a known function of h along the integration pathway. That function is provided by the additional constraint,

$$g'_{12}h_1^2 + g'_{23}h^2 = g'_{12}H_1^2 + g'_{23}H^2 + 2\frac{f^2}{\beta} \int_{x_e}^x w_{EK} dx, \quad (12)$$

where $H_1(y) \equiv h_1(x_e, y)$ and $H(y) \equiv h(x_e, y)$ are layer thicknesses along the eastern boundary. A useful property is that (12) is valid even in regions where $w'_1 > 0$.

2) ARRESTED FRONTS AND JETS

Since p_2 is proportional to h , the characteristic curves are streamlines for the layer-2 flow. Thus, there is layer-2 flow in the interior ocean only in regions reached by characteristics that originate from segments of the domain boundary along which h varies.

Characteristics can converge in the interior of the domain, or even intersect. In the latter case, if h varies along the domain boundary, there is a jump in h across the intersection, forming a stationary shock (an arrested front) and a jetlike current in layer 2 (Dewar 1991, 1992). Since the total transport field is in Sverdrup balance, it follows that there is also an oppositely directed jetlike current in layer 1,

$$h_1 u_1 = -\Psi_y - h_2 u_2, \quad h_1 v_1 = \Psi_x - h_2 v_2, \quad (13)$$

with a transport per width that exactly balances that of the layer-2 jet.

3) UPWELLING

According to (8b), the only mechanism for forcing a steady layer-2 circulation is upwelling by w'_1 . To help understand where upwelling is generated in the model, first consider the situation when there is no upwelling anywhere in the domain. In this case, the solution consists of a Sverdrup flow confined to layer 1, and h_1 has the structure $h_s(x, y)$ given by

$$\begin{aligned} h_s^2 &= H_1^2(y) + \frac{2}{g'_{12}} \frac{f^2}{\beta} \int_{x_e}^x w_{EK} dx \\ &= h_{10}^2 - \frac{2}{g'_{12}} \int_y^0 \tau^y dy + \frac{2}{g'_{12}} \frac{f}{\beta} \int_{x_e}^x \text{curl} \tau dx \\ &\quad + \frac{2}{g'_{12}} \int_{x_e}^x \tau^x dx, \end{aligned} \quad (14)$$

where $h_{10} \equiv h_1(x_e, 0)$. Equation (14) follows from (12) with the restriction that h is everywhere constant (i.e., no layer-2 flow), and the second equation of (8a) with $u_1 = 0$. The horizontal structure of h_s is determined by the wind. Its overall thickness is set by h_{10} , which must be large enough for the minimum value of h_s in the basin to be greater than or equal to h_{e1} (so that $w'_1 = 0$ everywhere). The h_1 fields plotted in the top panels of Figs. 6c and 10b below are approximations to h_s for their respective wind fields, but both are altered from h_s by w_1 .

In the theoretical solutions discussed below, h_{10} is usually set so that $h_s < h_{e1}$ somewhere in the domain. In the numerical solutions, transport M drains layer-1 water from the system, effectively decreasing h_{10} until h_1 becomes somewhere less than h_{e1} . Thus, upwelling must occur in both cases, and it happens in the neighborhood of regions where $h_s(x, y)$ is thinnest.

4) TRANSIENT PROCESSES

The preceding steady-state ideas also have a useful (albeit approximate) interpretation in transient situations. In response

to a switched-on wind, for example, first- and second-baroclinic ($n = 1$ and $n = 2$) Rossby waves radiate from the forcing region and from the eastern boundary. The $n = 1$ Rossby waves radiate westward, and adjust the total transport of the flow to be close to Ψ . This background Sverdrup flow then alters the propagation direction of the slower propagating $n = 2$ Rossby waves so that they propagate along characteristics rather than westward; that is, their zonal and meridional propagation velocities are given approximately by $c_{rx} = \bar{u}_g - c_r$ and $c_{ry} = \mathbf{v}_g$, respectively (Rhines 1985; McCreary et al. 1992; Liu 1999). The change in propagation direction can be severe; for example, McCreary et al. (1992) note the existence of eastward propagating $n = 2$ Rossby waves in their solution driven by τ^y winds when $\bar{u}_g > c_r$. Analyses of transients (not reported below) confirm that the model TJs in sections 3b(2) and 3c(2) are established by such Rossby wave adjustments.

b. Southern jet

Solutions for the southern TJ are forced by a wind field with two parts: a zonal wind stress τ^x extending throughout the entire basin to represent the southeast trades and a meridional wind stress τ^y confined to the eastern ocean to represent the upwelling-favorable winds along the South American coast. Each part has the separable form $\tau_o X(x)Y(y)$, and plots of $X(x)$ and $\tau_o Y(y)$ are provided in the top-left and bottom-left panels of Fig. 5, respectively. For these winds, w_{EK} is negative throughout the domain so that the only upwelling w'_1 in the system is coastal upwelling along the eastern boundary.

1) ANALYTIC SOLUTIONS

To solve (11) for the characteristics, boundary conditions are specified on the eastern edge of the domain at $x_e = 100^\circ$ and on the southern boundary at $y_s = 30^\circ\text{S}$. Along the eastern boundary, τ^y causes h_s to tilt upward toward the south. Coastal upwelling occurs whenever the tilt attempts to make $H_1 < h_{e1} = 80$ m, in which case w'_1 acts instantly to adjust it to h_{e1} . We assume that $H_1 = h_{e1}$ first at a prescribed latitude $y_1 = 5^\circ\text{S}$ so that upwelling occurs only poleward of y_1 . Equatorward of y_1 , $u_1 = u_2 = 0$ at the coast, and it follows from the second equations of (8a) and (8b) that

$$H(y) = H_o,$$

$$H_1(y) = \left(h_{e1}^2 + \frac{2}{g'_{12}} \int_{y_1}^y \tau^y dy \right)^{1/2}, \quad (15a)$$

where H_o is an as yet unspecified thickness. Poleward of y_1 , $h_2 u_2 = -h_1 u_1 = \tau^y / (g'_{23} h)$ at the coast, and we have

$$H_1(y) = h_{e1},$$

$$H(y) = \left(H_o^2 - \frac{2}{g'_{23}} \int_y^{y_1} \tau^y dy \right)^{1/2}. \quad (15b)$$

Along the southern boundary, we assume that there is no layer-2 flow. It follows that

$$h(x, y_s) = H(y_s),$$

$$h_1(x, y_s) = \left(H_1^2 + \frac{2}{g'_{12}} \frac{f^2}{\beta} \int_{x_e}^x w_{EK} dx \right)^{1/2}, \quad (16)$$

the first expression being a statement that there is no layer-2 flow and the second then following from constraint (12).

Figure 5 plots the characteristic curves calculated from (11) for different wind fields and parameters. Solution A1 (top-left panel) is forced only by τ^x and has $H = 1000$ m. Characteristics emerge from both eastern and southern boundaries with a slight northward tilt to the west owing to $\mathbf{v}_g > 0$, making $dy_c/ds > 0$. There is no layer-2 flow throughout the basin, however, because h is constant along the domain boundaries [i.e., $h(x, y_s) = H(y) = 1000$ m]. Solution A2 (top-right panel)

is the same as solution A1, except that the wind forcing also includes τ^y . Characteristics now bend somewhat more equatorward because \bar{u}_g , and hence dx_c/ds , is increased by the τ^y/f term. Since $H(y)$ decreases south of y_1 , h also decreases poleward in the interior ocean south of the characteristic that leaves the eastern boundary at y_1 , generating a broad eastward flow across the basin that carries layer-2 water to the eastern-boundary upwelling region.

Solution A3 (bottom-left panel) is the same as solution A2, except that H is reduced to 300 m. Characteristics now bend equatorward much more sharply, primarily because \bar{u}_g and \mathbf{v}_g are both increased by the decrease in h . They intersect in the interior ocean to form an arrested front, and a narrow eastward flow is generated along the convergence line, the solution's southern TJ. To indicate the approximate location of the front, we continue to plot characteristic curves after they intersect their neighbors, even though they are then no longer valid solutions to (11). [Dewar (1991, 1992) discusses how to solve for the precise location of the intersection.] Toward the east, the front shifts away from the equator and characteristics bend from the front to intersect the coast, indicating that layer-2 water leaves the jet to flow to the upwelling region. Finally, note that there are no characteristic curves that emerge from the southern boundary west of 50° . Conditions (16) cause h_1 to tilt down to the west; because H is now only 300 m, h_2 goes to zero thickness along y_s within the basin, and the integration of (11) breaks down.

Solution A4 is the same as solution A3 except $T_1 = 20^\circ\text{C}$ so that g'_{12} is reduced by 29%. The characteristics bend even more sharply to the north because c_r is reduced by the same factor. As a result, characteristics now appear to *intersect* the equator. Thus, the background stratification has a strong influence on where (or whether) the TJs converge onto the equator in the western ocean. In addition, note that characteristics do not leave the eastern boundary south of 25°S (bottom-right panel of Fig. 5). This is because $\bar{u}_g > c_r$ south of a critical latitude $y_{cr} = 26.6^\circ\text{S}$ so that $dx_c/ds < 0$ and $n = 2$ Rossby waves propagate *eastward* (see McCreary et al. 1992); indeed, characteristics that leave the southern boundary east of 97.5° (not shown) bend eastward to intersect the eastern boundary south of y_{cr} . Thus, in solution A4 there is a distinct TJ regime in the tropical ocean, defined by the region northeast of the southernmost characteristic that emerges from y_{cr} . (Conversely, y_{cr} also defines the northernmost edge of a subtropical coastal upwelling regime in which the source of upwelled water comes from farther south, rather than from the Tropics. The existence of such a cutoff was reported previously by Lu et al. 1998, who noted in their solution that subpolar water supplied the water for the coastal upwelling off California.)

2) NUMERICAL SOLUTIONS

Figure 6a shows a suite of numerical solutions (solutions N1–N4) that are analogous to solutions A1–A4, having the same forcings and stratification parameters. The panels plot the layer-2 current vector, $h_2\mathbf{v}_2 = (h_2u_2, h_2v_2)$, with shading to indicate regions of entrainment and detrainment by w_1 . Figure 6b plots $h_1\mathbf{v}_1$ and total transport, $h_1\mathbf{v}_1 + h_2\mathbf{v}_2$, fields for solution N3, and Fig. 6c plots its h_1 , h_2 , and h fields.


Solution N1 (top panel of Fig. 6a) is the solution when $\tau^y = 0$ and $\mathcal{H} = 1000$ m. In contrast to solution A1, there is layer-2 flow even though $\tau^y = 0$, driven by the throughflow transport $M = 5$ Sv. The inflow enters the basin at the southwest corner, moves to the equator in a western boundary current, flows along the equator into the eastern ocean, and upwells into layer 1 in the northeast corner of the basin.

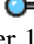
The h_s field driven by τ^x alone tilts upward toward the east along the equator so that h_s is thinnest along the eastern boundary, suggesting that upwelling should occur everywhere along the boundary. In solution N1, however, the upwelling weakens southward along the coast because there is no forcing mechanism to keep $h_1 < h_{e1}$ (since $\tau^y = 0$), and hence w_1 rapidly thickens h_1 to h_{e1} . Indeed, the meridional structure of h_1 along the coast is determined approximately by a balance between w_1 and the southward propagation of h_1 via coastal Kelvin waves; that is,

$$c_2 h_{1y} = w_1 = \frac{(h_{e1} - h_1)^2}{t_e h_{e1}}, \quad (17)$$



where c_2 is the Kelvin wave speed of the $n = 2$ baroclinic mode. The solution to (17) is

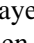
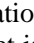
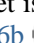
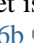

where y_o is set by specifying a value for h_1 at the equator that is less than h_{e1} . Thus, upwelling is present away from the equator at all only because w_1 has a finite value; that is, $t_e \neq 0$.

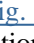


Solution N2 (upper-middle panel of [Fig. 6a](#) ) is the solution when τ^y is included. As for solution N1, the inflow first moves equatorward in a western boundary current but then, as for solution A2, it bends offshore before it reaches the equator, crossing the ocean in a broad interior flow to join an eastern-boundary upwelling region south of 7°S. The shift in the upwelling location away from the equator is implied by the structure h_s , which tilts upward along the eastern boundary when $\tau^y \neq 0$ so that its thinnest part is no longer located near the equator.


Solution N3 (lower-middle panel of [Fig. 6a](#) ) is the solution when \mathcal{H} is reduced to 300 m. In this case, some of the inflow (0.9 Sv) immediately entrains into layer 1 at the inflow port (shaded region at the southwest corner of the basin), a consequence of geostrophic adjustment to M . Subtracting the first equations of [\(8a\)](#) and [\(8b\)](#) and neglecting τ^y yields


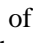
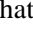
$$h_{1x} = -\frac{g'_{13}}{g'_{23}}h_{2x} = -\frac{fM}{g'_{12}h_2} \quad (19)$$

so that h_1 tilts upward (and h_2 and h tilt downward) to the west across the port ([Fig. 6c](#) ). Since h_1 remains close to h_{e1} along the southern boundary east of the port, a consequence of the balance $p_{ix} = 0$ approximately holding there, the tilt makes h_1 thinner than h_{e1} within the port and thereby forces the entrainment (top panel of [Fig. 6c](#) ). (This entrainment does not occur in solutions N1 and N2 because h_2 is larger, and hence h_{1x} is smaller, by a factor of about 3.)

The inflow in both layers first recirculates within the model's subtropical gyre. The layer-1 inflow (0.9 Sv) then moves to the equator in the interior ocean, and flows out of the basin through the exit port in the northwest corner of the basin ([Fig. 6b](#) ). In contrast, the inflow remaining in layer 2 (4.1 Sv) flows equatorward in a western-boundary current north of about 20°S. Consistent with solution A3, it then turns offshore near 4°S to flow eastward across the basin in a narrow jet, the model's southern TJ. The jet diverges from the equator in the eastern ocean, and water bends away from it to flow directly to the coastal upwelling region. These circulation features are all apparent in the structure of h , isolines of which are geostrophic streamlines for the layer-2 circulation (compare the lower-middle panel of [Fig. 6a](#) ) with the bottom panel of [Fig. 6c](#) ). Consistent with [\(13\)](#), a reverse jet is apparent in layer 1 (top panel of [Fig. 6b](#) ), and neither jet shows up in the total transport field (bottom panel of [Fig. 6b](#) ).

The total transport field (bottom panel of [Fig. 6b](#) ) is close to Sverdrup balance in the interior ocean, differing from that state only because of horizontal mixing. (Solutions N2 and N4 have the same total transport fields as solution N3. Solution N1 differs somewhat because it is not forced by τ^y .) There is a northward Sverdrup flow away from the southern boundary, and an eastward boundary current develops to provide water to compensate for this water loss. The presence of this eastward current in layer 2 is noteworthy since layer 2 is not directly forced by the wind. It exists there because \bar{u}_g is large enough to reverse the sign of dx_c/ds , which attains speeds greater than 5 cm s⁻¹ in a band centered about 27°S from the western boundary to 64°. This effect on the characteristics is apparent in the structure of h (bottom panel of [Fig. 6c](#) ): Isolines of h flow eastward from the inflow port and then circulate about the interior ocean. In contrast, for solution N2 \bar{u}_g is weaker by a factor of about 4, dx_c/ds attains speeds of only about 0.5 cm s⁻¹ in the aforementioned band, and it is negative near the western boundary; as a result, isolines from the eastern boundary fill the interior ocean, and there is no southern-boundary current (upper-middle panel of [Fig. 6a](#) ).

The eastward current is unrealistic, existing only because of the presence of the artificial southern boundary. To check its influence on solutions, we carried out a test run with $y_s = 40^\circ\text{S}$ and with τ^x and τ^y specified as shown in [Fig. 5](#) ) but extended farther south [i.e., south of 30°S, $Y(y)$ is $-\cos(\pi y/60^\circ)$ and 1, respectively]. The resulting solution was similar to Solution N7 north of 20°S, with a more fully developed subtropical gyre farther south. See [Lu et al. \(1998\)](#) and [McCreary and Lu \(2001\)](#) for discussions of analogous circulations in larger basins.

Solution N4 (bottom panel of [Fig. 6a](#) ) is similar to solution N3, except that the TJ intersects the equator because of the increase in \bar{u}_g caused by the decrease in g'_{12} . There is also a prominent band of detrainment along the southern flank of the TJ (red-shaded area in the bottom panel of [Fig. 6a](#) ) that adds 1.2 Sv to the TJ as it flows eastward. (There is a similar, but much weaker, band in solution N3 that is confined near the western boundary; lower-middle panel in [Fig. 6a](#) ) and

bottom panel in Fig. 6c (●).) To understand why this band exists, consider an application of (12) along some latitude, 7°S say. Values of h along the latitude are fixed by information propagating from the eastern and southern boundaries along characteristics, and $h \approx 300$ m along 7°S (similar to h for solution N3 in the bottom panel of Fig. 6c (●)). Constraint (12) requires that $\frac{1}{2}g'_{12}h^2_1 + \frac{1}{2}g'_{23}h^2_2$ increases across the basin, and h_1 must increase since h remains roughly constant.

Detrainment occurs if $h_2 < h_{c2}$ (i.e., $h_1 > h - h_{c2}$) at some point. The thickening of h_1 is more rapid for smaller g'_{12} , and hence the detrainment is stronger in solution N4. Although not applicable in our constant-density layer model, we note that such detrainment will act to lower the density of the TJ as it flows eastward, consistent with the observations (Johnson and Moore 1997; Rowe et al. 2000).

To investigate the TJ's dependence on M , we carried out a suite of test runs like solution N3 but with $M = 0, 2.5$, and 7.5 Sv. The $M = 2.5$ Sv and 7.5 Sv solutions were very similar in structure to solution N3, except with weaker or stronger upwelling along the eastern boundary, beginning at 13°S and 3°S, respectively, rather than at 7°S. In the $M = 0$ solution, the TJ existed for some time (20 years), but by year 40 it had essentially vanished.

c. Northern jet

Solutions for the northern TJ are found in the northern half-basin. They are forced by two idealized patches of zonal winds to represent the northeast trades: an “interior” one, τ^x , that extends throughout the entire basin and an “eastern” one, τ^x_e , confined to the eastern ocean. Again, each wind stress has the form $\tau_o X(x)Y(y)$. For the analytic solutions shown in Fig. 7 (●), plots of $X(x)$ and $\tau_o Y(y)$ for τ^x and τ^x_e are provided in the top-left and bottom-left panels, respectively, and we refer to them as the “analytic” winds. For the numerical solutions shown in Figs. 8a–c (●), the winds differ from the analytic ones in that $X(x)$ for τ^x decreases to zero at the western boundary and that τ_o for τ^x_e is strengthened from 0.5 to 0.75 dyn cm⁻²; we call them “numerical” winds.

Both τ^x and τ^x_e have regions of positive wind stress curl between the latitudes $y_1 = 5^\circ\text{N}$ and $y_2 = 13^\circ\text{N}$ to represent the ITCZ. For τ^x , however, the wind curl is not strong enough to reverse the sign of the Ekman pumping velocity w_{Ek} , which remains everywhere negative. When τ^x_e is included, w_{Ek} of the total wind field does become positive in the eastern interior ocean between y'_1 and y'_2 (6.4°N and 11.2°N for the analytic winds), defining a region in the interior ocean where open-ocean upwelling can occur (i.e., where $w'_1 \neq 0$). We define $x'_e(y)$ to be the boundary of the region, that is, the locus of points along which $w_{\text{Ek}} = 0$.

1) ANALYTIC SOLUTIONS

Layer thicknesses do not tilt along the eastern boundary of the basin ($x = x_e$) since $\tau^y = 0$, and so appropriate boundary conditions there are

$$H(y) = H_o, \quad H_1(y) = h_{e1}, \quad (20)$$

where H_o is as yet unspecified. The choice $H_1 = h_{e1}$ is both convenient (see below) and consistent with values of $h(x_e, y)$ from our numerical solutions. Along the northern boundary, we adopt conditions (16) with y_s replaced by y_n .

Since (9) is only valid where $w'_1 = 0$, we must determine a new eastern boundary for the integration domain that lies at the western edge of the upwelling region. For the wind field defined above, constraint (12) implies that $\frac{1}{2}g'_{12}h^2_1 + \frac{1}{2}g'_{23}h^2_2$ decreases away from the eastern boundary for $x > x'_e$. Because h_1 cannot be thinner than h_{e1} and $H_1 = h_{e1}$, it follows that

$$h_1(x, y) = h_{e1} \quad (21a)$$

everywhere in the region $x > x'_e$, and hence by (12) that

$$h(x, y) = \left(H_o' + \frac{g'_{23}}{f} w_{\text{Ek}} \int_{x_e} dx \right), \quad (21b)$$

there. The upwelling velocity w'_1 is then related to w_{Ek} and to $h_2 \mathbf{v}_2$ by

$$w'_1 = \frac{h_2}{h} w_{\text{Ek}} = \frac{\beta}{f} h_2 \mathbf{v}_2, \quad (21c)$$

which follow from (8a–c) and the property that $h_1 = h_{e1}$. Since $w'_1 \propto w_{\text{Ek}}$, (21c) identifies $x'_e(y)$ as being the desired boundary of the integration domain, and (21a) and (21b) evaluated at $x = x'_e$ provide the required layer thicknesses along the domain boundary. According to (21b), $h(x'_e, y)$ varies from H_o at y'_1 and y'_2 to a minimum h_m at some latitude y_m between them, and it is because of this property that the integration of (9) allows nonzero layer-2 flow to exist elsewhere in the basin. (A straightforward generalization of the above method allows x'_e to be found for other choices of winds and with $H_1 > h_{e1}$, for which the upwelling region is separated from the eastern boundary.)

Figure 7 plots characteristic curves calculated from (11) for various idealized wind fields and boundary conditions. Solution A5 (top-left panel) is forced only by the interior zonal wind τ^x with $H = 1000$ m. Analogous to solution A1, characteristics emerge from both the eastern and northern boundaries with a slight southward tilt to the west owing to $\mathbf{v}_g < 0$ making $dy_c/ds < 0$, and there is no layer-2 flow anywhere in the basin since $h = H_o$ everywhere along the boundary. Solution A6 (top-right panel) is the same as solution A5, except that τ^x_e is included so that there is now an upwelling region in the eastern ocean between y'_1 and y'_2 (shaded area). As a consequence, characteristic curves begin at its western edge x'_e rather than x_e , and isolines of h determined from (21b) are plotted within the upwelling region. The h field attains a minimum value $h_m = 993.5$ m along x'_e at $x_m = 62^\circ$, $y_m = 9.0^\circ\text{N}$. Thus, there is geostrophic flow *into* the upwelling region along the characteristics that emerge from x'_e in the latitude band $y'_1 \leq y < y_m$ (band 1) and flow *out of* the upwelling region along the characteristics for $y_m \leq y < y'_2$ (band 2), forming a recirculation around the upwelling region within layer 2.

According to (21c), the layer-2 meridional transport for $x > x'_e$ across latitude y is given by

$$\mathcal{V}(y) = \int_{x'_e}^{x_e} h_2 \mathbf{v}_2 dx = \frac{1}{2} \frac{g'_{23}}{f} [H_2^2 - h_2^2(x'_e, y)], \quad (22)$$

where $H_2 = H - H_1$, and the upwelling transport south of y is

$$\mathcal{W}(y) = \int_{y'_1}^y dy \int_{x'_e}^{x_e} \frac{h_2}{h} w_{\text{Ek}} dx = \int_{y'_1}^y \frac{1}{y} \mathcal{V}(y) dy. \quad (23)$$

It follows from mass conservation that the inflow transport in band 1 is $\mathcal{U}^+ = \mathcal{V}(y_m) + \mathcal{W}(y_m)$, the total upwelling is $\mathcal{W}(y'_2) \equiv \tilde{\mathcal{W}}$, and $\mathcal{R} = \mathcal{U}^+ - \tilde{\mathcal{W}}$ is the outflow transport in band 2, the latter being the strength of the recirculation. Values of these transports for solution A6 are $\mathcal{V}(y_m) = 3.91$ Sv, $\mathcal{W}(y_m) = 0.77$ Sv, $\mathcal{U}^+ = 4.7$ Sv, $\tilde{\mathcal{W}} = 1.2$ Sv, and $\mathcal{R} = 3.5$ Sv. Note that the recirculation \mathcal{R} is considerably stronger than the upwelling $\tilde{\mathcal{W}}$ that drives it. This property can be understood from the structure of \mathcal{W} in (23), which implies that the ratio $\mathcal{V}(y_m)/\tilde{\mathcal{W}} \geq [\ln(y'_2/y'_1)]^{-1} = 1.8$. [See Spall (2000) for a detailed discussion of such upwelling-driven recirculations.]

In solution A7 (bottom-left panel), H is reduced to 300 m. Characteristics north of y'_2 now bend much more sharply toward the equator, but they are blocked by the ITCZ where w_{Ek} becomes weak and \mathbf{v}_g small. Characteristics from the

western edge of the upwelling region extend westward, then bend southwest westward south of y_1 . Some of them have an eastward-directed portion, a consequence of c_r becoming small enough for \bar{u}_g to reverse sign as h_2 thins (h_1 thickens) toward the west. Similar to solution A6, h attains a minimum value $h_m = 277.6$ m at y_m , again defining bands of eastward and westward layer-2 flow. Characteristics for band 1 intersect in the western ocean forming an arrested front associated with eastward flow, the model's northern TJ. Interestingly, some curves from band 2 bend southward to be close to the TJ, forming a westward counterflow on its poleward edge. The TJ, recirculation, and upwelling transports are $\mathcal{U}^+ = 3.7$ Sv, $\bar{\mathcal{W}} = 1.0$ Sv, and $\mathcal{R} = 2.7$ Sv, smaller values than those for solution A6 because the ratio h_2/h is smaller.

Solution A8 (bottom-right panel) is the same as solution A7 except that $T_1 = 20^\circ\text{C}$. Characteristics have similar pathways to those in solution A7 but the TJ bends more sharply toward the equator, a consequence of g'_{12} and hence c_r being smaller in dx_c/ds . Indeed, some appear to intersect the equator in the interior ocean. There is also a portion of $x'_e(y)$ from which no characteristics emerge because the characteristic velocity is directed into the upwelling region. Along this boundary segment, some characteristics from farther along the boundary bend back to intersect x'_e (as one of the curves in the bottom-right panel almost does), forming a front and boundary current along $x'_e(y)$.

We also obtained an analogous suite of solutions (solutions A5'–A8'), forced by the numerical winds defined at the beginning of [section 3c](#) for which the upwelling region is strengthened and broadened, its western edge extending to $x_m = 53^\circ$. The solutions are similar to those in [Fig. 7](#), except that for solutions A6' and A7' characteristics loop back much more strongly in the ITCZ band and the portion of $x'_e(y)$ from which no characteristics emerge extends north of y_m . For later reference, we note that $\mathcal{U}^+ = 10.0$ Sv, $\bar{\mathcal{W}} = 3.0$ Sv, and $\mathcal{R} = 7.0$ Sv for solution A6', which weaken to 7.7, 2.3, and 5.4 Sv, respectively, for solution A7'.

2) NUMERICAL SOLUTIONS

[Figure 8a](#) plots $h_2\mathbf{v}_2$ vectors and w_2 fields for a suite of numerical solutions (solutions N5–N8) forced by the numerical winds, but otherwise comparable to solutions A5–A8. Solutions N6–N8 have unstable currents, and fields averaged over 360 days are shown for these solutions. [Figure 8b](#) plots $h_1\mathbf{v}_1$ and total-transport vectors for solution N5. [Figure 8c](#) plots instantaneous h for solution N6, and 360-day averaged h fields for solutions N6 and N7.

Solution N5 (top panel of [Fig. 8a](#); [Fig. 8b](#)) is the solution when $\tau^x_e = 0$ and $\mathcal{H} = 1000$ m. The total transport field (bottom panel of [Fig. 8b](#)), which is close to being in Sverdrup balance, has a subtropical gyre driven by negative curl north of y_2 and both a North Equatorial Counter Current (NECC) and intensified NEC driven by wind curvature in the ITCZ band. There is no upwelling in the ITCZ band since w_{Ek} is everywhere negative without τ^x_e , but, as in solution A5, there is upwelling in the eastern equatorial and coastal ocean driven by $M = 5$ Sv. The inflow M enters the basin at the southwest corner, flows eastward along the equator (top panel of [Fig. 8a](#)), upwells into layer 1 in the eastern ocean, returns to the western ocean as an equatorial current (top panel of [Fig. 8b](#)), and finally exits the basin from 2° to 6°N along the western boundary. Consistent with [\(13\)](#), the two equatorial currents do not appear in the total transport field (bottom panel of [Fig. 8b](#)).

Solution N6 (upper-middle panel of [Fig. 8a](#)) is the solution when τ^x_e is included. In contrast to solution N5, most of the upwelling now occurs in the band of negative w_{Ek} ($\bar{\mathcal{W}} = 3.2$ Sv in the region $x < 95^\circ$, $y > 5^\circ\text{N}$) so that the equatorial and coastal upwelling is much reduced (1.8 Sv). This shift in upwelling location is consistent with the h_s structure for this wind, which is now thinnest in the region where $w_{\text{Ek}} > 0$. Consistent with solution A6, there are eastward and westward currents just south and north of the upwelling region that extend across the basin, and there is northward flow across the upwelling band. The westward current bends southward at the western boundary and then joins the eastward one, forming a basinwide recirculation gyre (upper-middle panel of [Fig. 8a](#), middle panel of [Fig. 8c](#)).

The westward current becomes unstable in a band west of the upwelling regime centered about 13°N , generating unstable waves that propagate westward across the basin with a wavelength of about 500 km and a period of about 75 days (top panel of [Fig. 8c](#)). The h_1 field (not shown) is sharply tilted across the band due to forcing by w_{Ek} , suggesting that the waves are generated by a type of baroclinic instability. This idea is supported by the property that the waves are also present in layer 1, but shifted toward the east against the vertical shear. The waves are also tilted against the layer-1 horizontal shear,

suggesting that a type of barotropic instability may be active. (Recall that the 2½-layer model does not include momentum advection, and so lacks terms that are important in both instability types. We carried out a test run like solution N6 but with the advection terms retained in the momentum equations and the solution was much the same, with only the wavelength and period of the instabilities being somewhat shorter.) Similar unstable waves are present in solutions N7 and N8, but not in solution N5, likely because h_1 tilts less in the eastern ocean since there is no τ_e^x .

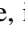
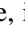


The amplitude of the waves is large enough to affect the mean flow field significantly, strengthening the westward current in association with the development of eastward recirculations to either side. The layer-2 eastward current north of 12°N, for example, is a residual flow due entirely to the waves (upper-middle panel of Fig. 8a , middle panel of Fig. 8c ). The eastward current south of 12°N is both driven by the eastern ocean upwelling and strengthened by the waves.

Figure 9  plots various transport curves across the basin, defined by

$$\begin{aligned}\mathcal{E}(x) &= \int_0^{4^\circ\text{N}} h_2 u_2^+ dx, \\ \mathcal{U}^+(x) &= \int_0^{12^\circ\text{N}} h_2 u_2^+ dx - \mathcal{E}(80^\circ), \\ \mathcal{U}^-(x) &= \int_{6^\circ\text{N}}^{17^\circ\text{N}} h_2 |u_2^-| dx, \\ \mathcal{R}(x) &= \mathcal{U}^-(x) - \int_{12^\circ\text{N}}^{30^\circ\text{N}} h_2 u_2^+ dx, \quad (24)\end{aligned}$$

where u_2^+ (u_2^-) is the positive (negative) part of u_2 . The transports measure the strengths of the eastward, equatorial (\mathcal{E} , dotted curve) and off-equatorial (\mathcal{U}^+ , solid curve) currents and the westward (\mathcal{U}^- , dot-dashed curve) current, respectively. Transport \mathcal{R} (dashed curve) estimates the strength of the westward flow *without* the contribution associated with the wave-driven recirculation to its north (so that $\mathcal{U}^- - \mathcal{R}$ measures the strength of the northern recirculation itself).

Transport \mathcal{E} has the constant value of 1.8 Sv in the eastern ocean west of 90°W, in agreement with the amount of equatorial and coastal upwelling reported above. In response to the Ekman pumping, \mathcal{U}^+ and \mathcal{R} both gradually increase away from the eastern boundary to about 62°, where their values (9 and 5.5 Sv) approach those predicted by the analytic model forced by the numerical winds (10 and 7 Sv). Note also that their difference, $\mathcal{U}^+(x) - \mathcal{R}(x)$, which is equal to the amount of upwelling east of x , gradually increases to about 3.2 Sv near 62°, close to the upwelling transport predicted analytically (3.0 Sv). From 62° to 50°, \mathcal{U}^+ and \mathcal{R} increase rapidly by 7 Sv to 16 and 12 Sv, and remain near these strengths farther to the west. This increase occurs too far west to be forced by the Ekman pumping, and it therefore must be driven by the unstable waves. Interestingly, there are energetic waves in the real ocean in this latitude band, which appear to be generated both locally by instabilities and remotely by the propagation of wind-driven anticyclones from the coasts of Mexico and Central America (Enfield 2001, personal communication; Giese 2001, personal communication).

Solution N7 (lower-middle panel of Fig. 8a ) is the solution when \mathcal{H} is reduced to 300 m. The overall flow field is similar to that of solution N6, except that the eastward jet in layer 2 now shifts equatorward toward the west to form the model's northern TJ. A prominent difference from solution N6 is that the westward extent of the upwelling band is less and the upwelling transport \bar{W} is much reduced (1.5 Sv), more than predicted analytically (2.3 Sv). The cause of these changes appears to be advection of thicker h_2 into the $w_{\text{EK}} < 0$ region, which is much stronger in solution N7 since h_2 is thinner and hence \mathbf{v}_2 larger. (This weakening does not occur in solution A7 because, by assumption, w_1' is strong enough to maintain $h_1 = h_{e1}$ regardless of the strength of \mathbf{v}_2 .) As in solution N6, \mathcal{U}^+ and \mathcal{R} increase steadily away from the eastern boundary to about 7 and 6 Sv near 77° in response to the Ekman pumping, and then strengthen abruptly to 9 and 8 Sv from 77° to 73° owing to the development of unstable waves. These values are close to those of solution A7' (7.7 and 5.4 Sv), rather surprising given the large modifications caused by advection and the unstable waves.

Another difference from solution N6 is that solution N7 has a subtropical gyre in layer 2, with a strong eastward current

along the northern boundary (compare upper- and lower-middle panels in [Fig. 8a](#) and middle and bottom panels in [Fig. 8c](#)). As for the analogous change between solutions N2 and N3, its cause is h_2 being thinner by a factor of 4, which decreases c_r , increases \bar{u}_g , and strongly reverses the sign of dx_c/ds . In solution N3, inflow through the southern boundary maintains the layer-2 subtropical gyre. In solution N7, however, the subtropical gyre appears to be separated from the IOC-driven circulation farther south so that the only possible forcing mechanism is the unstable waves. [Another possibility is that the layer-2 subtropical gyre is a transient feature that is decaying very slowly: Since $\bar{u}_g > c_r$ in the northern subtropics, there is an enclosed area there into which $n = 2$ Rossby waves cannot propagate ([Rhines and Young 1982](#)); as a result, any circulation inside this region can spin down only through horizontal mixing, a very slow decay process ([McCreary et al. 1992](#)). There is, however, no indication that the gyre is decaying even after 200 years of integration.]

Solution N8, for which $T_1 = 20^\circ\text{C}$, is similar to solution N7 except that its TJ bends more sharply to the equator owing to the reduction in g'_{12} and c_r , and its off-equatorial upwelling ($\bar{W} = 1.1$ Sv) and TJ transport (7.5 Sv) weaken even more. There is detrainment along the poleward edge of the TJ (3.0 Sv: red band in the bottom panel of [Fig. 8a](#)), which exists for the same reasons as for the southern TJ in solutions N3 and N4; that is, h is fixed to be close to 250 m near the equator, and constraint (12) then requires h_1 to thicken until $h_2 < h_{e2}$. This detrainment strengthens both the TJ and the equatorial jet, the latter attaining a maximum transport of 6.0 Sv.

To investigate the solutions' dependence on M , we carried out a suite of test runs like solution N7 but with $M = 0, 2.5,$ and 7.5 Sv. The $M = 2.5$ and 7.5 Sv solutions were almost unchanged from solution N7 away from the equator. For example, the upwelling strengths in the ITCZ band for the two solutions were 1.5 Sv and 1.4 Sv, respectively, and their TJ strengths were 10 Sv and 9 Sv. The change in M values is thus taken up almost entirely by altering the strength of equatorial upwelling and the equatorial jets to 1 Sv and 5.5 Sv. The reason is that the *maximum* amount of upwelling that can take place in the ITCZ band is fixed by (21c) and limited further by h_2 advection. The values of M are all beyond this maximum, so the excess must be taken up elsewhere (i.e., along the equator).

Surprisingly, in the $M = 0$ solution a strong recirculation gyre and TJ (7 Sv) remained, even though there was *no upwelling* anywhere in the basin. Its driving mechanism appears to be the downward transfer of energy from layer 1 to layer 2 by unstable waves, which are still continuously generated along 13°N . With $M = 0$, layer 1 continues to entrain layer-2 water until h_1 is thick enough to eliminate w_1 altogether. After this adjustment, h_1 has a state very much like h_s , with its thinnest value lying within the ITCZ band where $w_{\text{Ek}} > 0$. Because the mean h_1 and h_2 fields are therefore still similar to those of solution N7, characteristic curves have similar pathways in the two solutions and, consequently, similar structures for the recirculation gyre, including a northern TJ. As noted in [section 4a\(3\)](#), however, this property holds only for the $2\frac{1}{2}$ -layer model, as the northern TJ and recirculation gyre vanish when $M = 0$ in the $4\frac{1}{2}$ -layer model.

4. Solutions to the $4\frac{1}{2}$ -layer model

One limitation of the $2\frac{1}{2}$ -layer model is that it does not have enough vertical resolution to be able to simulate a realistic equatorial current structure, that is, one with an EUC flanked by deeper TJs ([Fig. 1](#)). Another is that because no mass transfer is allowed across the bottom of the TJ layer (i.e., $w_2 = 0$), its overall thickness, a critical parameter for determining characteristic pathways, is set *externally* by specifying \mathcal{H}_2 . Here, we report solutions to the $4\frac{1}{2}$ -layer model, which generates an EUC primarily in layer 2, develops TJs in layer 3, and determines the layer-3 thickness *internally* (since $w_3 \neq 0$). Solutions are also obtained in the full tropical basin and are forced by monthly [Hellerman and Rosenstein \(1983\)](#) winds, modified as discussed in [section 2a\(4\)](#) except for the test solution reported in [section 4a\(5\)](#). As we shall see, although the $4\frac{1}{2}$ -layer model lacks the simplicity of the $2\frac{1}{2}$ -layer one, the basic TJ dynamics nevertheless appear to be the same in both systems.

Most of the results reported here also occur in solutions to a $3\frac{1}{2}$ -layer version of the model, which is the same as the $4\frac{1}{2}$ -layer one except without layer 4 and with $w_3 = 0$. Like the $2\frac{1}{2}$ -layer model, however, the $3\frac{1}{2}$ -layer model has the theoretically unpleasant property that, because $w_3 = 0$, the thickness of the TJ layer is determined externally by specifying \mathcal{H}_3 [see [section 4a\(3\)](#)].

a. Annual-mean circulations

[Figures 10a](#) and [10b](#) present the annually averaged solution for the parameters stated in [section 2a](#), our “main run,” plotting $h_i v_i$ and w_i in the former and $h_1, h_2, h_3,$ and $p'_3 = p_3/g'_{35} = h_1 + h_2 + h_3 + (g'_{45}/g'_{35})h_4$ in the latter, where p_3 is the layer-3 pressure. Isolines of p'_3 are geostrophic streamlines for layer 3, so p'_3 provides an alternate picture of the

overall layer-3 flow field. The p_3 field is analogous to acceleration potential on a density surface near the TJ core, and its similarity to [Fig. 2](#) is striking. In addition, [Fig. 3](#) shows the layer structure of the main run at 140°W, which compares favorably with the observed temperature structure in [Fig. 1](#).

1) LAYERS 1 AND 2

Consistent with the observed circulation, the layer-1 and layer-2 flow fields (top and upper-middle panels of [Fig. 10a](#)) have subtropical gyres in each hemisphere, an NECC that shifts equatorward toward the west, a weak SECC in the far-western ocean near 10°S, and an EUC. In addition, the EUC is shifted slightly south of the equator in the eastern ocean, a response to the southerly component of the wind there (see, e.g., [Philander and Delecluse 1983](#); [Yu et al. 1997](#)). There is also eastward flow along the equator in layer 1 from 140°W to 100°W, an indication of the surfacing of the EUC by upwelling. The subtropical gyres are closed by eastward currents along the northern and southern boundaries, and there is upwelling along these artificial boundaries because $\tau^x \neq 0$ there; however, these unrealistic features do not significantly affect the solution (see the discussion of solution N3).



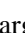


Water for the EUC is supplied primarily by the north and south subtropical cells (STCs; [McCreary and Lu 1994](#); [Liu and Philander 1995](#)). In these cells, layer-1 water subducts in the subtropics due to w_d (red-shaded areas in the upper-middle panel of [Fig. 10a](#) for $|y| > 15^\circ$), flows to the equator in layer 2, upwells in the eastern tropical ocean (blue areas in the upper-middle panel of [Fig. 10a](#); dark-blue areas in the top panel of [Fig. 10b](#)), and eventually returns to the subtropics in layer 1. North and south tropical cells (TCs) also contribute to the EUC. They are analogous to the STCs but their descending branches are located within the Tropics, generated by w_{c2} in regions where $h_2 < h_{c2}$ (red-shaded areas in the upper-middle panel of [Fig. 10a](#) and dark-blue areas in upper-middle panel of [Fig. 10b](#), both for $|y| \leq 15^\circ$). Indeed, most of the downward flow associated with the TCs occurs 2°–3° on either side of the equator, a result of the convergence of Ekman transport away from the equator caused by the increase of $|f|$ [i.e., $(h_1 \mathbf{u}_1)_y = (\beta/f^2)\tau^x$], which thickens h_1 and thins h_2 there (top panel of [Fig. 10a](#), upper two panels of [Fig. 10b](#)).


2) LAYERS 3 AND 4

As for the layer-2 circulation in solution N3, some of the layer-3 inflow from the IOC (1.0 Sv) first entrains into layer 2, and thereafter follows several different possible pathways in layers 1 and 2 before exiting the basin ([Lu et al. 1998](#)). The rest (7.0 Sv) circulates about the South Pacific subtropical gyre, flows to the equator in a western-boundary current, and turns offshore to flow eastward near the equator (lower-middle panel of [Fig. 10a](#), bottom panel of [Fig. 10b](#)). The layer-4 inflow (2 Sv) circulates about a deep portion of the subtropical gyre, somewhat smaller in size than the one in layer 3, flows equatorward along the Australian and New Guinea coasts and either recirculates within the Southern Hemisphere (0.9 Sv) or crosses into the Northern Hemisphere near the western boundary (1.1 Sv). It eventually mixes upward into layer 3 (light-blue area in the bottom panel of [Fig. 10a](#)) almost entirely by w_{m3} wherever h_3 is relatively thin (dark-blue areas in the lower-middle panel of [Fig. 10b](#)).

The layer-3 flow field has three distinct eastward currents in the Tropics that are clearly linked to upwelling regions in the eastern ocean (blue-shaded regions in the lower-middle panel of [Fig. 10a](#)). The currents and regions are a southern TJ with a maximum transport of about 4 Sv driven mostly by coastal and open-ocean upwelling near the South American coast (3.4 Sv for the region east of 95°W and from 3° to 30°S); a northern TJ with a maximum transport of about 6 Sv linked to open-ocean upwelling in the Costa Rica Dome (0.8 Sv east of 110°W and from 5°N to 15°N) and a second region farther west (0.7 Sv for 160°W–110°W, 5°N–15°N); and a jet located just south of the equator forced by upwelling along the equator (2.2 Sv for 160°W–110°W, 2°S–2°N) and along 2.5°S (0.9 Sv for 130°W–90°W, 2°S–5°S). Consistent with solutions A3 and N3, the southern TJ shifts poleward toward the east and layer-3 water bends away from the jet in the eastern ocean to flow to the South American upwelling region. Consistent with solutions A7 and N7, the northern TJ is significantly strengthened by a basinwide recirculation, with its eastward-flowing branch extending across the ocean near 13°N.

[Figure 3](#) helps to illustrate the reason for the upwelling band along 2.5°S. The $h_1 + h_2$ field is thin on either side of the EUC near 2.5°S and 2.5°N and, because of the southerly winds, it is thinner at 2.5°S. This meridional asymmetry is greater farther to the east, where the southerly winds are stronger. As a result, $h_1 + h_2$ becomes less than $h_{e1} + h_{e2} = 80$ m in a band in the eastern ocean near 2.5°S but not near 2.5°N, and layer-3 water upwells only south of the equator to drive the near-equatorial jet. It is tempting to interpret this jet as the primary southern TJ in [Fig. 1](#), but it is located somewhat too close to the equator, and so it is perhaps better to view it as being a deep portion of the EUC. Thus, a southern TJ with two distinct cores is not reproduced in the solution's annual-mean flow field.

Similar to solution N7, there is a Northern Hemisphere subtropical gyre in layer 3 (lower-middle panel of [Fig. 10a](#) , bottom panel of [Fig. 10b](#) ) . In this solution, however, it results from h_3 being close to h_{c3} and hence there being little or no geostrophic shear between layers 2 and 3 so that $\mathbf{v}_2 \approx \mathbf{v}_3$ (dark blue area north of 15°N in the lower-middle panel of [Fig. 10b](#) ) . There are also large-amplitude unstable waves along the eastward branch of the recirculation gyre, and the weak layer-3 flow on its northern side is an indication of their influence. Their effect on the layer-4 flow is even more apparent, where they drive a deep extension of the eastward branch with westward counterflows on either side (bottom panel of [Fig. 10a](#) ) . Layer 4 also has a weak subtropical gyre north of 20°N , which is also likely forced by the unstable waves (see the discussion of solution N7). Another possibility is that it is driven by the entrainment of layer-4 water into layer 3 via w_{m3} (bottom panel of [Fig. 10a](#) ) . The layer-4 circulation is not significantly changed in a test solution with $w_{m3} = 0$ [see [section 4a\(4\)](#)], however, indicating that w_{m3} is not its primary forcing mechanism.



A final noteworthy Northern Hemisphere flow is the eastward current in layer 3 along near 17°N from 140°W to the coast of Mexico (lower-middle panel of [Fig. 10a](#) ) . It is driven by the coastal upwelling there (1.0 Sv for $x > 125^\circ\text{W}$, $y > 20^\circ\text{N}$), and its dynamics are similar to those for the southern TJ. As indicated by the p_3 field, it is supplied mostly by water from the southward branch of the North Pacific subtropical gyre, which then retroflects to flow to the coast.

3) SENSITIVITY TO M

In a test solution with $M = 0$, both TJs vanish after an initial adjustment period of about 30 years. Although unstable waves still remain in the 13°N band, they are considerably weaker than in solution N7, and apparently are not able to sustain the northern TJ and recirculation gyre. A likely reason for this difference from solution N7 is that wave energy is not trapped to the TJ layer in the $4\frac{1}{2}$ -layer model, but rather radiates into the deeper ocean (i.e., into layer 4).

To investigate the influence of the IOC vertical structure, we obtained test solutions with $\Phi = 0.5$ and 1.0. In the $\Phi = 0.5$ solution (for which the inflow is 5 Sv in both layers 3 and 4), the circulation was almost unchanged from the main run but h_3 was a bit thinner almost everywhere, allowing w_{m3} to entrain the additional 3 Sv of layer-4 inflow into layer 3. In the $\Phi = 1$ solution (for which the inflow is all in layer 3), however, $h_1 + h_2 + h_3$ was thicker near the equator by about 50 m, which among other things shifted the TJs farther from the equator. When $\Phi < 1$, the outflow drains more layer-1 and layer-2 water from the domain (M) than can be supplied by the layer-3 inflow (ΦM): The model responds by thinning layer 3 until $w_{m3} + w_{c3}$ is large enough when integrated over the basin to entrain all the layer-4 inflow $[(1 - \Phi)M]$. When $\Phi = 1$, this internal mechanism for thinning h_3 does not exist, and the overall thickness of h_3 is rather determined externally through the specification of \mathcal{H}_3 .

4) SENSITIVITY TO W_2 AND W_3

To investigate the influence of our vertical mixing parameterizations, we obtained six test solutions: with $\epsilon = 0$ and 0.5, $\delta = 0$ and 0.5, and $\kappa = 0$ and $0.1 \text{ cm}^2 \text{ s}^{-1}$ [defined in [Eqs. \(1\)](#) and [\(5\)](#)]. The choice of ϵ hardly affects solutions at all because w_{m3} ensures that $h_3 > h_{c3}$ and, hence, $w_{c3} = 0$ almost everywhere in the basin; in addition, the locations where $h_3 < h_{c3}$ tend to coincide with regions where $h_2 < h_{e2}$ (middle panels of [Fig. 10b](#) ) and in that case the terms proportional to ϵ are removed from w_2 and w_3 [[Eq. \(1\)](#)]. In contrast, the choice of δ alters solutions strongly, the TJs being eliminated in the two tests. When $\delta = 0$ or 0.5, layer-3 water can upwell into layer 2 wherever $h_2 < h_{e2}$, and it does so mostly in the bands 2° – 3° lat on either side of the equator where h_2 is thin (lower-middle panel of [Fig. 10b](#) ) . As a result, the off-equatorial upwelling regions that drain the TJs in the main run are eliminated, and the TJs are replaced by an equatorial jet (see [Lu et al. 1998](#)).



Solutions are also sensitive to the strength of w_{m3} through its effect on $h_1 + h_2 + h_3 \equiv h_{123}$. With $\kappa = 0.1 \text{ cm}^2 \text{ s}^{-1}$, h_{123} along the tropical eastern boundary and throughout the equatorial ocean increases from about 290 m in the main run to 320 m. Consistent with the analytic results and half-basin solutions, the model TJs did not converge toward the equator as much in the western ocean, intersecting the western boundary near 5°S and 5°N . Conversely, with $\kappa = 0$, h_{123} decreased to 240 m and the TJs converged onto the equator near the date line.



5) SENSITIVITY TO T

To explore the model's sensitivity to τ , we obtained a test solution forced by the unmodified [Hellerman and Rosenstein](#)

(1983) winds, which have equatorial easterlies that are 30% larger than they are in the main run [see [section 2a \(4\)](#)]. The amount of layer-3 water that upwelled along the equator increased from 2.2 Sv in the main run to 5.7 Sv in the test, strengthening the equatorial jet considerably. Conversely, the amount of upwelling in each of the off-equatorial regions (including the southwestern corner of the basin and off Mexico) decreased by 0.5–0.9 Sv. In particular, the open-ocean upwelling in the Northern Hemisphere (Costa Rica Dome and west of it) weakened from 1.5 Sv to 0.6 Sv and the upwelling near South America decreased from 3.3 Sv to 2.6 Sv. Thus, the structure of τ affects the model TJs by altering the relative strengths of the equatorial and off-equatorial upwelling regions.


b. Annual cycle


To illustrate the annual variability of the TJs, [Fig. 11](#)  plots bimonthly snapshots of $h_3 \mathbf{v}_3$ for the main run from 15°S to 15°N. Three bands of eastward currents (red bands) are present in the eastern ocean in most of the panels, although they are often broken into separate segments by instabilities. The two outer bands correspond to the northern and southern TJs in the annual-mean flow field, following similar pathways across the basin. The middle band is located along the equator during the latter half of the year. From March to July, however, it is located south of the equator, close to the location of the primary southern TJ in [Fig. 1](#) . In the Southern Hemisphere, the time-varying currents are not visible in layers 1 or 2, supporting their interpretation as higher-order ($n > 1$) Rossby waves radiating from the coast. In the Northern Hemisphere, this interpretation is not so clear because of similar variations of the NECC in layer 1.





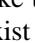

Note that there is also a westward equatorial current in [Fig. 11](#)  (blue shading) during the latter half of the year, the only current in the model that resembles the EIC. This flow does not appear in the annual-averaged flow field (lower-middle panel of [Fig. 10a](#) ) and results from reflected, higher-order Rossby waves.

5. Summary and discussion

An hierarchy of models of intermediate complexity (2½-layer and 4½-layer systems) is used to investigate TJ dynamics. Solutions are found in idealized and realistic basins, and they are obtained analytically and numerically. They are forced both by winds and by the Pacific IOC, the latter consisting of a prescribed outflow M (usually either 5 or 10 Sv) of upper-layer water through the western boundary or far-western equator (for the southern half-basin), and a compensating deep inflow of lower-layer water through the southern boundary.

Analytic solutions to the 2½-layer model [[Eq. \(8\)](#)] suggest that the TJs are geostrophic currents along arrested fronts. Information about the structure of h along domain boundaries is propagated into the interior ocean along characteristic curves, x_c and y_c , determined by integrating [Eq. \(11\)](#). Arrested fronts are generated when characteristics associated with different h values converge or intersect ([Dewar 1991, 1992](#)). The solutions indicate further that the southern and northern TJs are driven by upwelling in the eastern ocean near and along South America and in the ITCZ band, respectively, that the northern TJ is part of a recirculation gyre that extends across the basin (upper-right and bottom panels of [Fig. 7](#) ) and that the TJ pathways are sensitive to the stratification parameters, H and g_{12} .

Numerical solutions to the 2½-layer model confirm the analytic results and show that the northern TJ is strengthened considerably by unstable waves that develop along the eastward branch of the recirculation gyre (top panel of [Fig. 8c](#) ). They also identify the role of the IOC in driving the TJs: It essentially drains upper-layer water from the system until h_1 is thin enough to require layer-2 water to upwell into layer 1. Interestingly, in a solution with $M = 0$, the southern TJ vanishes but the northern one remains, being driven by the unstable waves. This property suggests an alternate forcing mechanism for the recirculation gyre and northern TJ, namely, eddy–mean flow interaction. On the other hand, there are no TJs in the $M = 0$ solution to the 4½-layer model, likely because the unstable waves along 13°N, which might otherwise maintain the northern TJ, radiate energy downward into layer 4. Thus, this mechanism in the 2½-layer model may only be an artifact of its reduced vertical resolution.

Solutions to the 4½-layer model demonstrate that TJs, dynamically similar to those in the 2½-layer model, still exist in a system with a realistic upper-ocean circulation, one that includes both the EUC and STCs [[section 4a\(1\)](#)]. Indeed, the circulations in the TJ layer (layer 3) are to a large extent a combination of the layer-2 flows in the two half-basin solutions (compare lower-middle panels of [Figs. 6a](#) , [8a](#) , and [10a](#) ). In contrast to solution N3, however, the equatorial jet in the 4½-layer solution is shifted south of the equator by the southerly winds. In addition, part of the northern TJ that circulates about the Costa Rica Dome is linked to an upwelling regime along the Mexican coast (bottom panel of [Fig. 10b](#) ). Finally, a primary TJ (like the current near 4.5°S in the top panel of [Fig. 1](#) ) is not a distinct feature in the annual-mean flow field but it does exist in the annual cycle, being most prominent from April to July ([Fig. 11](#) ).

The 4½-layer solutions are not sensitive to the vertical structure of the prescribed inflow, provided that there is some inflow in layer 4 (i.e., $\Phi < 1$). In that case, the outflow drains upper-layer water from the domain until w_{m3} (and w_{c3}) are

large enough to entrain all the layer-4 inflow into layer 3. Thus, when $\Phi < 1$, the overall thickness of layer 3 is determined internally rather than externally as the layer-2 thickness is in the 2½-layer model. Solutions are also not sensitive to the vertical-mixing parameter ϵ primarily because w_{m3} keeps $h_3 > h_{c3}$. In contrast, they are quite sensitive to δ , the TJs being replaced by an equatorial jet if $\delta \neq 1$; in that case, layer-3 water upwells into layer 2 mostly in two bands where $h_2 < h_{c2}$ located 2°–3° on either side of the equator, and upwelling regions that drive the TJs in the main run are eliminated. They are also sensitive to the strength of w_{m3} through its influence on h_{123} : When κ is decreased, the TJs converge more toward the equator in the western ocean and vice versa. Finally, the wind stress τ used to force the model affects the TJs by determining the relative strengths of upwelling in the equatorial and off-equatorial regions. When the model is forced by the full-strength [Hellerman and Rosenstein \(1983\)](#) winds, for example, the amount of equatorial upwelling more than doubles, and all the off-upwelling regions weaken to compensate for this increase.

If the processes discussed here are the primary ones involved in TJ dynamics, then it is understandable why TJs have been difficult to simulate in GCMs. First, the GCM must include the Pacific IOC, which has been done only recently with the advent of fully global solutions. Second, vertical mixing must be weak enough in the interior ocean to allow the development of a realistic thermocline layer. The GCM's vertical-mixing parameterization must also allow for upwelling in off-equatorial regions since, otherwise, all upwelling will occur on the equator and the TJs collapse to become a deep part of the EUC. In this regard, it is noteworthy that TJs are best developed in GCMs with the highest vertical resolution, such as the JAMSTEC model. Finally, the wind field that is used to force the GCMs is also critical, as regions of off-equatorial wind curl tend to be too weak in most products, and the equatorial wind stress is too strong in some (e.g., the [Hellerman and Rosenstein 1983](#), winds).

Processes, other than the ones we focus on in this paper, may also be involved in TJ dynamics. For example, midlatitude subduction can also transfer upper-layer water down to the depths of SPLTW (layer 3), providing an additional mechanism for draining upper-layer water from the system other than the IOC. If midlatitude subduction is involved, the TJs are part of a meridional overturning cell confined within the Pacific, one analogous to the STCs but extending somewhat deeper and to higher latitudes. In other proposed mechanisms, the TJs are viewed essentially as an equatorially trapped phenomenon with no direct link to the larger-scale circulation. These mechanisms include local vertical-mixing processes (Marin et al. 1999) and near-equatorial recirculations with strong eddy–mean flow interactions (as may be occurring in the JAMSTEC solution).

It is noteworthy that there are subsurface countercurrents in the Atlantic Ocean as well, and any of the mechanisms mentioned in the previous paragraph could be their cause. Regarding the processes discussed in this paper, we note that the Atlantic's deep thermohaline circulation (DTC) may play an analogous role to the Pacific's IOC. The DTC is an overturning circulation in which intermediate water enters the South Atlantic, flows into the North Atlantic as near-surface water, is cooled there and sinks to form North Atlantic Deep Water, and eventually flows southward to exit the basin. As such, the DTC also acts to drain upper-layer water from the Tropics, thereby establishing the need for upwelling in off-equatorial regions.

In conclusion, we have obtained solutions to a suite of intermediate ocean models that are able to generate TJs comparable with observations in a number of aspects. Perhaps the most important implications of these solutions are that the TJs are driven by off-equatorial upwelling and that they are an essential branch of the IOC. If the latter proves true, it is a remarkable example of remote forcing on a basinwide scale. A limitation of the models we have used is their parameterization of vertical mixing, which is determined only by layer thicknesses. It is useful, then, that some GCMs with more realistic vertical-mixing parameterizations are now able to simulate TJs. These solutions, however, have not yet been fully analyzed to isolate TJ dynamics, so it is not yet known if the ideas discussed here are also at work in them. Finally, we had hoped that our solutions would also make a steady-state EIC, since it has been suggested that it is dynamically related to the TJs ([Rowe et al. 2000](#)). It is likely that determining this relationship (or lack of it) will provide further clues for understanding the TJs themselves as well as basic equatorial dynamics.

Acknowledgments

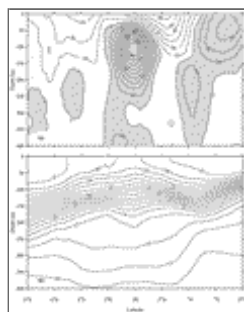
This research was sponsored by NSF Grant OCE-98-11261 and by the Frontier Research System for Global Change through its sponsorship of the International Pacific Research Center. Part of this work was done while Julian McCreary was at Nova Southeastern University and Zuojun Yu was at JISAO, University of Washington. Discussions with Eric Firing, Akio Ishida, Greg Johnson, Billy Kessler, Kevin Kohler, and Dennis Moore were very helpful. We further thank Greg Johnson for preparing [Figs. 1](#) and [2](#) and Billy Kessler for providing us his updated version of the [McCreary \(1981\)](#) linear, continuously stratified model. The programming and data-analysis assistance of the Ferret group at NOAA PMEL is greatly appreciated.

REFERENCES

- Bingham F., and R. Lukas, 1995: The distribution of intermediate water in the western equatorial Pacific during January–February, 1986. *Deep-Sea Res.*, **42**, 1545–1573. [Find this article online](#)
- Dewar W. K., 1991: Arrested fronts. *J. Mar. Res.*, **49**, 21–52. [Find this article online](#)
- Dewar W. K., 1992: Spontaneous shocks. *J. Phys. Oceanogr.*, **22**, 505–522. [Find this article online](#)
- Donohue K. A., E. Firing, G. D. Rowe, A. Ishida, and H. Mitsudera, 2002: Equatorial Pacific subsurface countercurrents: A model/data comparison in stream coordinates. *J. Phys. Oceanogr.*, **32**, 1252–1264. [Find this article online](#)
- Godfrey J. S., 1989: A Sverdrup model of the depth-integrated flow for the World Ocean, allowing for island circulations. *Geophys. Astrophys. Fluid Mech.*, **45**, 89–112.
- Harrison D. E., 1989: On climatological monthly mean wind stress and wind stress curl fields over the World Ocean. *J. Climate*, **2**, 57–79. [Find this article online](#)
- Hellerman S., and M. Rosenstein, 1983: Normal monthly wind stress over the world ocean with error estimates. *J. Phys. Oceanogr.*, **13**, 1093–1104. [Find this article online](#)
- Ishida A., Y. Kushino, H. Mitsudera, N. Yoshioka, and T. Kadokura, 1998: Preliminary results of a global high-resolution GCM experiment. *J. Fac. Sci. Hokkaido Univ., Ser. VII*, **11**, 441–460. [Find this article online](#)
- Johnson G. C., and D. W. Moore, 1997: The Pacific subsurface countercurrents and an inertial model. *J. Phys. Oceanogr.*, **27**, 2448–2459. [Find this article online](#)
- Johnson G. C., and M. J. McPhaden, 1999: Interior pycnocline flow from the subtropical to the equatorial Pacific Ocean. *J. Phys. Oceanogr.*, **29**, 3073–3089. [Find this article online](#)
- Johnson G. C., and E. Firing, 2001: Equatorial Pacific Ocean horizontal velocity, divergence, and upwelling. *J. Phys. Oceanogr.*, **31**, 839–849. [Find this article online](#)
- Kitamura Y., and N. Suginoara, 1987: Effect of vertical viscosity and diffusivity on tropical ocean circulation. *J. Oceanogr. Soc. Japan*, **43**, 1–20. [Find this article online](#)
- Kraus E. B., and J. S. Turner, 1967: A one-dimensional model of the seasonal thermocline. II: The general theory and its consequences. *Tellus*, **19**, 98–106. [Find this article online](#)
- Liu Z. Y., 1999: Forced planetary wave response in a thermocline circulation. *J. Phys. Oceanogr.*, **29**, 1036–1055. [Find this article online](#)
- Liu Z. Y., and S. G. H. Philander, 1995: How different wind stress patterns affect the tropical–subtropical circulations of the upper ocean. *J. Phys. Oceanogr.*, **25**, 449–462. [Find this article online](#)
- Lu P., J. P. McCreary, and B. A. Klinger, 1998: Meridional circulation cells and source waters of the Pacific Equatorial Undercurrent. *J. Phys. Oceanogr.*, **28**, 62–84. [Find this article online](#)
- Lukas R., 1986: The termination of the equatorial undercurrent in the eastern Pacific. *Progress in Oceanography*, Vol. 16, Pergamon, 63–90.
- Luyten J. R., and H. Stommel, 1986: Gyres driven by combined wind and buoyancy flux. *J. Phys. Oceanogr.*, **16**, 1551–1560. [Find this article online](#)
- Luyten J. R., J. Pedlosky, and H. Stommel, 1983: The ventilated thermocline. *J. Phys. Oceanogr.*, **13**, 292–309. [Find this article online](#)
- Maltrud M. E., R. Smith, A. Semtner, and R. Malone, 1998: Global eddy-resolving ocean simulations driven by 1985–1995 atmospheric winds. *J. Geophys. Res.*, **103**, 30825–30854. [Find this article online](#)
- Marin F., B. L. Hua, and S. Wacongne, 2000: The equatorial thermostat and subsurface countercurrents in the light of atmospheric Hadley cells dynamics. *J. Mar. Res.*, **58**, 405–437. [Find this article online](#)
- McCreary J. P., 1981: A linear stratified ocean model of the equatorial undercurrent. *Philos. Trans. Roy. Soc. London*, **A298**, 603–635. [Find this article online](#)
- McCreary J. P., and P. Lu, 1994: Interaction between the subtropical and the equatorial oceans: The subtropical cell. *J. Phys. Oceanogr.*, **24**, 466–497. [Find this article online](#)
- McCreary J. P., 2001: Influence of the Indonesian Throughflow on the circulation of intermediate water in the Pacific Ocean. *J. Phys. Oceanogr.*, **31**, 932–942. [Find this article online](#)

- McCreary J. P., Y. Fukamachi, and P. Lu, 1992: A nonlinear mechanism for maintaining coastally trapped eastern boundary currents. *J. Geophys. Res.*, **97**, 5677–5692. [Find this article online](#)
- McPhaden M. J., 1984: On the dynamics of equatorial subsurface countercurrents. *J. Phys. Oceanogr.*, **14**, 1216–1225. [Find this article online](#)
- Philander S. G. H., and P. Delecluse, 1983: Coastal currents in low latitudes. *Deep-Sea Res.*, **30**, 887–902. [Find this article online](#)
- Reid J. L. Jr., 1965: Intermediate waters of the Pacific Ocean. *Johns Hopkins Oceanogr. Stud.*, No. 2, 85 pp.
- Rhines P. B., 1986: Vorticity dynamics of the oceanic general circulation. *Annu. Rev. Fluid Mech.*, **18**, 433–497. [Find this article online](#)
- Rhines P. B., and W. R. Young, 1982: A theory of the wind-driven circulation. I: Mid-ocean gyres. *J. Mar. Res.*, **40**, 559–596, (Suppl.). [Find this article online](#)
- Rowe G. D., E. Firing, and G. C. Johnson, 2000: Pacific equatorial subsurface countercurrent velocity, transport, and potential vorticity. *J. Phys. Oceanogr.*, **30**, 1172–1187. [Find this article online](#)
- Spall M. A., 2000: Buoyancy-forced circulations around islands and ridges. *J. Mar. Res.*, **58**, 957–982. [Find this article online](#)
- Toggweiler J. R., K. Nixon, and W. S. Broecker, 1991: The Peru upwelling and the ventilation of the South Pacific thermocline. *J. Geophys. Res.*, **96**, 20467–20497. [Find this article online](#)
- Tsuchiya M., 1972: A subsurface north equatorial countercurrent in the eastern Pacific Ocean. *J. Geophys. Res.*, **77**, 5981–5986. [Find this article online](#)
- Tsuchiya M., 1975: Subsurface countercurrents in the eastern equatorial Pacific Ocean. *J. Mar. Res.*, **33**, 145–175, (Suppl.). [Find this article online](#)
- Tsuchiya M., 1981: The origin of the Pacific equatorial 13°C water. *J. Phys. Oceanogr.*, **11**, 794–812. [Find this article online](#)
- Tsuchiya M., 1991: Flow path of the Antarctic Intermediate Water in the western equatorial South Pacific Ocean. *Deep-Sea Res.*, **38**, 273–279, (Suppl.). [Find this article online](#)
- Tsuchiya M., R. Lukas, R. A. Fine, E. Firing, and E. Lindstrom, 1989: Source waters of the Pacific equatorial undercurrent. *Progress in Oceanography*, Vol. 23, Pergamon, 101–147.
- Wyrski K., and B. Kilonsky, 1984: Mean water mass and current structure during the Hawaii-to-Tahiti Shuttle Experiment. *J. Phys. Oceanogr.*, **14**, 242–254. [Find this article online](#)
- Yu Z., P. S. Schopf, and J. P. McCreary, 1997: On the annual cycle in the eastern Pacific Ocean. *J. Phys. Oceanogr.*, **27**, 309–324. [Find this article online](#)
- Yu Z., J. P. McCreary, W. S. Kessler, and K. A. Kelly, 2000: Influence of equatorial dynamics on the Pacific North Equatorial Countercurrent. *J. Phys. Oceanogr.*, **30**, 3179–3190. [Find this article online](#)

Figures



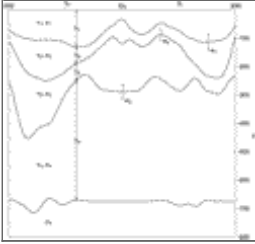
[Click on thumbnail for full-sized image.](#)

FIG. 1. Mean distributions of zonal flow (top) and temperature (bottom) at 135°W. Contour intervals are 10 cm s^{-1} and 1°C . The TJs are the eastward currents on either side of the equator located along thermal fronts present at the poleward edges of thermoclast water from 150 to 500 m. A secondary TJ is located about 8°S . [After [Johnson et al. \(2001\)](#)]



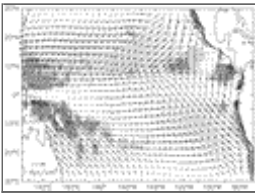
Click on thumbnail for full-sized image.

FIG. 2. Acceleration potential (dynamic meters) relative to 900 dbar on the 26.5 kg m^{-3} neutral density surface, which lies in a depth range from about 300 to 400 m in the tropical Pacific Ocean. Regions where the acceleration potential is less than 11.5, 11.4, and 11.3 J kg^{-1} are indicated by light, medium, and dark shadings, respectively. Isolines tend to recirculate in the Northern Hemisphere but to intersect the eastern boundary in the Southern Hemisphere. [After [Johnson and McPhaden \(1999\)](#)]



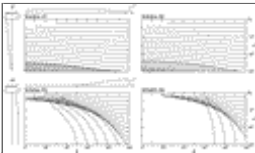
Click on thumbnail for full-sized image.

FIG. 3. A section along 140°W from the main run, illustrating the structure of the model. Various quantities are defined in the text



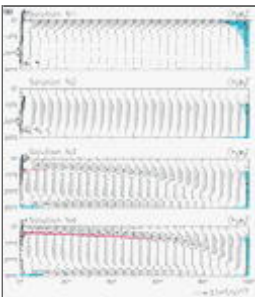
Click on thumbnail for full-sized image.

FIG. 4. Annual-mean winds from the [Hellerman and Rosenstein \(1983\)](#) climatology, modified as discussed in [section 2a\(d\)](#). Shading indicates where the Ekman pumping velocity w_{Ek} is positive; the outer boundary for the lightest shading is $10^{-4} \text{ cm s}^{-1}$, and other shading boundaries are 5×10^{-4} , 10^{-3} , and $5 \times 10^{-3} \text{ cm s}^{-1}$



Click on thumbnail for full-sized image.

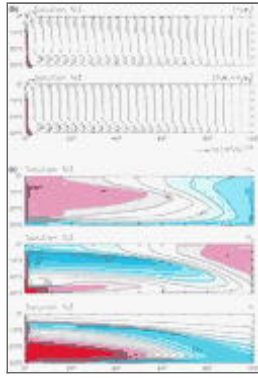
FIG. 5. Characteristics for solutions A1–A4, calculated from (11) for various wind fields and specified layer thicknesses along the eastern and southern boundaries, as described in the text. The $X(x)$ and $\tau_o Y(y)$ structures for the τ^x and τ^y wind fields are indicated in the top-left and bottom-left panels, respectively



Click on thumbnail for full-sized image.

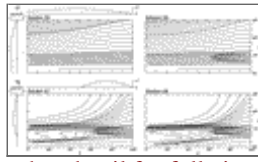
FIG. 6. (a) Horizontal distributions of $(h_2 \mathbf{v}_2)'$ (arrows) and w_1 (shading) fields for solutions N1–N4. To emphasize weaker flows, current arrows are of the vector field $(h_2 \mathbf{v}_2)' \equiv h_2 \mathbf{v}_2 / |h_2 \mathbf{v}_2|^{1/2}$ rather than $h_2 \mathbf{v}_2$ itself. Positive (negative) values of w_1 are shown by blue (red) shading, and the lightest shadings indicate where w_1 is greater than 0.1 cm day^{-1} or less than -0.1 cm day^{-1} . (b) Horizontal distributions of $(h_1 \mathbf{v}_1)'$ (top) and $(h_1 \mathbf{v}_1 + h_2 \mathbf{v}_2)'$ (bottom) for solution N3. To emphasize weaker flows, current

arrows are of the vector fields $(h_1 \mathbf{v}_1)' \equiv h_1 \mathbf{v}_1 / |h_1 \mathbf{v}_1|^{1/2}$ and $(h\mathbf{v})' \equiv h\mathbf{v}/|h\mathbf{v}|^{1/2}$ where $h\mathbf{v} = h_1 \mathbf{v}_1 + h_2 \mathbf{v}_2$. (c) Horizontal distributions of h_1 , h_2 , and h fields for solution N3. Contour intervals are 20 m for h_1 and h_2 , and 10 m for h . Red (blue) shading indicates where layers are thicker (thinner)



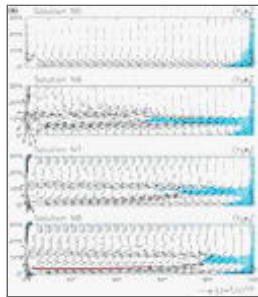
[Click on thumbnail for full-sized image.](#)

FIG. 6. (Continued)



[Click on thumbnail for full-sized image.](#)

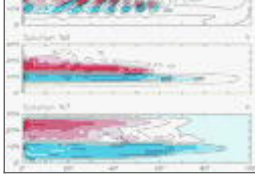
FIG. 7. Characteristics for solutions A5–A8, calculated from (11) for various wind fields and specified layer thicknesses along the eastern boundary x'_e and northern boundary, as described in the text. The region of open-ocean upwelling is indicated by shading, and isolines of h determined from (21b) are also plotted there. For the shaded regions, contour intervals for h are (top-right) 1 m and (bottom-right) 2.5 m, and the additional contours of 999.75 and 299.75 m are also included. The $X(x)$ and $\tau_o Y(y)$ structures for the τ^x and τ^y wind fields are indicated in the top-left and bottom-left panels, respectively



[Click on thumbnail for full-sized image.](#)

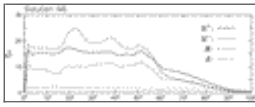
FIG. 8. (a) Horizontal distributions of $(h_2 \mathbf{v}_2)'$ (arrows) and w_1 (shading) fields, showing solutions N5–N8. To emphasize weaker flows, current arrows are of the vector field $(h_2 \mathbf{v}_2)' \equiv h_2 \mathbf{v}_2 / |h_2 \mathbf{v}_2|^{1/2}$ rather than $h_2 \mathbf{v}_2$ itself. The fields for solutions N6–N8 are averaged over 360 days due to the presence of unstable waves. Positive (negative) values of w_1 are shown by blue (red) shading, and the lightest shadings indicate where w_1 is greater than 0.1 cm day^{-1} or less than -0.1 cm day^{-1} . (b) Horizontal distributions of $(h_1 \mathbf{v}_1)'$ (top) and $(h_1 \mathbf{v}_1 + h_2 \mathbf{v}_2)'$ (bottom) for solution N5. To emphasize weaker flows, current arrows are of the vector fields $(h_1 \mathbf{v}_1)' \equiv h_1 \mathbf{v}_1 / |h_1 \mathbf{v}_1|^{1/2}$ and $(h\mathbf{v})' \equiv h\mathbf{v}/|h\mathbf{v}|^{1/2}$ where $h\mathbf{v} \equiv h_1 \mathbf{v}_1 + h_2 \mathbf{v}_2$. (c) Horizontal distributions of instantaneous h for solution N6 (top) and 360-day averaged h fields for solution N6 (middle) and solution N7 (bottom). Contour intervals in the top, middle, and bottom panels are 10, 5, and 20 m, respectively. Red (blue) shading indicates where h is thicker (thinner)





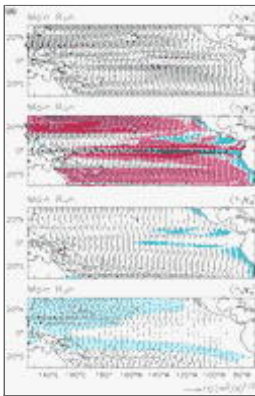
Click on thumbnail for full-sized image.

FIG. 8. (Continued)



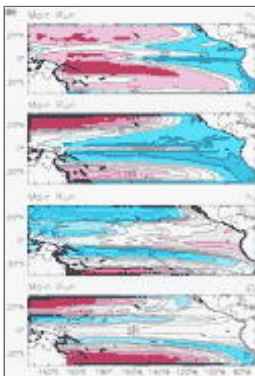
Click on thumbnail for full-sized image.

FIG. 9. Transports across the basin for solution N6, showing curves for U^+ (solid), R (dashed), E (dotted), and U (dot-dashed) fields, as defined in (24)



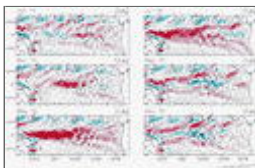
Click on thumbnail for full-sized image.

FIG. 10a. Horizontal distributions of $(h_i v_i)'$ (arrows) and w_i (shading) fields for the main run. To emphasize weaker flows, current arrows are of the vector field $(h_i v_i)' \equiv h_i v_i / |h_i v_i|^{1/2}$. The w_1 , w_2 , and w_3 fields are shown in the upper-middle, lower-middle, and bottom panels, respectively. Positive (negative) values of w_1 are shown by blue (red) shading, and the lightest shadings indicate where w_i is greater than 0.1 cm day^{-1} or less than -0.1 cm day^{-1}



Click on thumbnail for full-sized image.

FIG. 10b. Horizontal distributions of h_1 , h_2 , h_3 , and $p_3' = p_3/g'_{35}$ fields for the main run. The contour interval is 20 m for all panels, except in the blue region of the bottom panel where it is 10 m. Red (blue) shading indicates where layers are thicker (thinner)



Click on thumbnail for full-sized image.

FIG. 11. Horizontal distributions of $(h_3 \mathbf{v}_3)'$ (arrows) and $h_3 u_3$ (shading) fields for the main run, illustrating its annual cycle. To emphasize weaker flow, current arrows are of the vector field $(h_3 \mathbf{v}_3)' \equiv h_3 \mathbf{v}_3 / |h_3 \mathbf{v}_3|^{1/2}$. Red (blue) shading highlights regions where $h_3 u_3 \geq (\leq) 5 \text{ m}^2 \text{ s}^{-1}$

* SOEST Contribution Number 5931 and International Pacific Research Center Contribution Number 146.

Corresponding author address: Dr. Julian P. McCreary, International Pacific Research Center, School of Ocean and Earth Science and Technology, University of Hawaii, 2525 Correa Road, Honolulu, HI 96822. E-mail: jay@soest.hawaii.edu

top ▲



© 2008 American Meteorological Society [Privacy Policy and Disclaimer](#)
Headquarters: 45 Beacon Street Boston, MA 02108-3693
DC Office: 1120 G Street, NW, Suite 800 Washington DC, 20005-3826
amsinfo@ametsoc.org Phone: 617-227-2425 Fax: 617-742-8718
[Allen Press, Inc.](#) assists in the online publication of AMS journals.